Engineering Structures

Novel crack-width visual measurement based on backbone double-scale features for improved detection automation

--Manuscript Draft--

Manuscript Number:	ENGSTRUCT-D-22-01654R1
Article Type:	VSI:Machine Learning in SE
Keywords:	Concrete crack; Image thinning; Machine vision; Multi-scale feature fusion
Corresponding Author:	Yunchao Tang Zhongkai University of Agriculture and Engineering Guangzhou, Guangdong CHINA
First Author:	Yunchao Tang
Order of Authors:	Yunchao Tang
	Zhaofeng Huang, Master
	Zheng Chen, Ph.D.
	Mingyou Chen
	Hao Zhou, Master
	Hexin Zhang, Ph.D.
	Junbo Sun, Ph.D.
Manuscript Region of Origin:	Asia Pacific
Abstract:	State-of-the-art machine-vision systems have limitations associated with crack width measurements. The sample points used to describe the crack width are often subjectively defined by experimenters, which obscures the crack width ground truth. Consequently, in most related studies, the uncontrollable system errors of vision modules result in unsatisfactory measurement accuracy. In this study, the cracks of a reservoir dam are taken as objects, and a new crack backbone refinement algorithm and width-measurement scheme are proposed. The algorithm simplifies the redundant data in the crack image and improves the efficiency of crack-shape estimation. Further, an effective definition of crack width is proposed that combines the macroscale and microscale characteristics of the backbone to obtain accurate and objective sample points for width description. Compared with classic methods, the average simplification rate of the crack backbone and the average error rate of direction judgment are all improved. The results of a series of experiments validate the efficacy of the proposed method by showing that it can improve detection automation and has potential engineering application.
Suggested Reviewers:	Qingfeng Liu, Ph.D. Associate Professor, Shanghai Jiao Tong University liuqf@sjtu.edu.cn related expert in deep learning
	Jian Yang Professor, University of Birmingham j.yang.3@bham.ac.uk senior expert in vision detection and deep learning technology
	Lijuan Li Professor, Guangdong University of Technology lilj@gdut.edu.cn senior expert in vision method
	Bing Fu, Ph.D. Professor, Jinan University fubing@jnu.edu.cn related expert in crack detection

	Bassam Tayeh Associate Professor, Islamic University of Gaza btayeh@iugaza.edu.ps Related expert in deep learning
	Aref Abadl Associate Professor, King Saud University aabadel@ksu.edu.sa Related expert in machine learning
Opposed Reviewers:	
Response to Reviewers:	

Declaration of interests

☒ The authors declare that they have no known competing financial interests or personal relationships that could have appeared to influence the work reported in this paper.

☐The authors declare the following financial interests/personal relationships which may be considered as potential competing interests:

Highlights

- Backbone neighborhood distribution points are reduced to facilitate classification.
- Dual-scale backbone features are combined for accurate width measurement direction.
- A detailed visual measurement process of crack width is proposed, providing stable and continuous measurement.
- A visual measurement method of crack width that is closer to reality is used to obtain more accurate results.
- Two evaluation standards of measurement (i.e., recall rate and direction error) are added to enable a more comprehensive evaluation of the measurement method.

Novel visual crack width measurement based on backbone double-scale features for improved detection automation

Yunchao Tang[1,2,3*], Zhaofeng Huang[4], Zheng Chen[1,2*], Mingyou Chen[4], Hao Zhou[4], Zhang Hexin[5], Sun Junbo[6]

[1] *Guangxi Key Laboratory of Disaster Prevention and Engineering Safety, School of Civil Engineering and Architecture, Guangxi University, Nanning 530004, China*;

[2] *Key Laboratory of Disaster Prevention and Structural Safety of Ministry of Education, School of Civil Engineering and Architecture, Guangxi University, Nanning 530004, China*;

[3] *College of Urban and Rural Construction, Zhongkai University of Agriculture and Engineering, Guangzhou, Guangdong* 510006, *China;*

[4] *College of Engineering, South China Agricultural University, Guangzhou, Guangdong* 510642, *China;*

[5] *School of Engineering and the Built Environment, Edinburgh Napier University, 10 Colinton Road, Edinburgh, Scotland, UK, EH10 5DT*

[6] *School of Design and Built Environment, Curtin University, Perth, WA 6102, Australia;*

Abstract: State-of-the-art machine-vision systems have limitations associated with crack width measurements. The sample points used to describe the crack width are often subjectively defined by experimenters, which obscures the crack width ground truth. Consequently, in most related studies, the uncontrollable system errors of vision modules result in unsatisfactory measurement accuracy. In this study, the cracks of a reservoir dam are taken as objects, and a new crack backbone refinement algorithm and width-measurement scheme are proposed. The algorithm simplifies the redundant data in the crack image and improves the efficiency of crack-shape estimation. Further, an effective definition of crack width is proposed that combines the macroscale and microscale characteristics of the backbone to obtain accurate and objective sample points for width description. Compared with classic methods, the average simplification rate of the crack backbone and the average error rate of direction determination are all improved. The results of a series of experiments validate the efficacy of the proposed method by showing that it can improve detection automation and has potential engineering application.

Key words: Concrete crack; Image thinning; Machine vision; Multi-scale feature fusion

1 Introduction

Cracks are a common type of structural damage that jeopardize the health of concrete buildings (e.g., roads, bridges, tunnels, and dams) [1–5]. Regular inspections and repairs can reduce the risk of structural collapse during natural disasters (e.g., earthquakes and floods) [6–10].

Researchers have proposed a variety of innovative methods to replace traditional manual visual inspection [11–14]. However, their methods target larger, more complex field-environment crack detection tasks that are expensive, slow and susceptible to external interference [15–18] . Non-contact, high-precision computer-assisted visual measurement has shown good performance in various inspection fields [19–23] and is a promising method to replace human visual inspections. Researchers have provided a relatively complete process framework for mapping image pixel features to geometric dimensions in real physical space [24,25] . However, for complex slender and irregular targets, such as cracks, the current measurement applications lack geometric meaning, and their accuracy is not sufficient [26].

Regarding the identification and segmentation of cracks, researchers have applied the classic digital image processing (DIP) method and neural-network models to make the extraction of cracks more robust [27–32]. Kim et al. [33] compared the threshold segmentation effects of five classic threshold segmentation algorithms on concrete cracks and showed that the less robust threshold segmentation suffers background complexity, large changes in illumination, and inconsistencies. It is generally difficult to accurately detect cracks under uniform conditions. Other researchers have proposed semantic segmentation models that have been effective in solving these problems [34–37]. Many scholars have also proposed corresponding model structures specifically for crack detection. For example, Zou et al. developed the DeepCrack [27] network based on SegNet and achieved an F-measure greater than 0.87. They improved the segmentation accuracy but introduced larger scale parameters. Ju et al. developed the CrackU-net [38] model, which improved on U-Net and FCN and achieved an accuracy of 99.01%. Wang and Cheng combined DilaSeg and RNN and proposed DilaSeg-CRF [29] for segmentation cracks, which achieved a 20% to 32% improvement compared to the classic semantic segmentation model. Zhang et al. designed CrackNet [39] without a pooling layer in an attempt to reduce the accuracy loss in the crack segmentation process. Then, they combined it with an RNN and proposed CrackNet-R [28] to improve the accuracy of segmentation, subsequently obtaining a higher recall rate and F-measure. These neural-network methods were optimized for concrete cracks and provided more opportunities for improvement. However, increasing the network depth to improve accuracy increases the burden on the hardware in the application process.

The quantitative analysis of crack-hazard degree (e.g., crack length, width, and depth) is presently insufficient [17,40] . For example, clearly defining a crack width from a visual measurement and continuously performing such measurements remain quite challenging [26,41,42]. Historically, researchers used an edge or a skeleton of the crack as the basis for width measurement [43], but several problems remain. For example, the two edges of a crack may be quite different in the local area, and it is difficult to obtain accurate measurement directions. The crack skeletons obtained by improved refinement algorithms must still handle redundant data, and the definition of the skeleton remains inaccurate.

Researchers have attempted to use these features to define the crack-width visual measurement method and achieved varying results. For example, Asjod et al. [44] proposed the arc-length method to measure cracks. Further, Wang et al. [26] proposed a Laplace-based continuous explicit measurement method that simulates the crack as an electric field in a capacitor, and used the total length of the trajectory of electrons in the cathode and anode of a capacitor to define the width of the crack. However, the width obtained by their method is the length of a curve, not a straight-line distance needed for engineering. Kim et al. [45] proposed using the two edge points closest to the crack skeleton point for width measurement. Luo et al. [46] investigated the crack edges from the crack skeleton point in four directions and took the minimum distance between the two edges in the four directions as the width of the crack. Their method performs well with idealized cracks. However, in reality, the width often refers to the straight-line distance between the two edges in the normal direction of the crack-growth direction, and the crack edges often have irregular bumps. Hence, the two edges are not strictly symmetrical about the skeleton.

The above methods use measurement points that do not match the geometric meaning of width. Therefore, the measurement correctness must be improved. The comprehensiveness of using only numerical results as the evaluation criteria of measurement methods needs to be improved. In addition, whereas many studies have focused on road cracks, only a few have focused on dam cracks, which have characteristics of large image noise, complex background texture, and random location [47,48]. The research object needs to be expanded, thus, a large scope exists for machine-vision measurement research in this area.

In this study, we selected a reservoir dam crack located in the field as the research object and developed a more streamlined crack backbone extraction algorithm, based on an improved image-refinement algorithm, that enhances the backbone's ability to describe crack shapes. Further, we devised a more accurate measurement direction by combining the backbone macroscale slope characteristics and microscale neighborhood distribution characteristics. Then, defining the width of the crack as the straight-line distance between two measurement points located at the edge of the crack in the measurement direction, we developed a crack-width measurement method. Two evaluation criteria are included: the measurement recall rate and direction error. Compared with the method proposed by Luo et al. [46], the method proposed here is more comprehensive, in that it has a more accurate visual measurement performance that aligns with the geometric meaning of width. This study makes the following contributions:

1. A detailed visual crack width measurement process is proposed that can provide stable and continuous measurements.

2. Based on the improved image-refinement algorithm used to further refine the complete crack backbone, the neighborhood distribution types of backbone points are reduced to facilitate their use in classifying backbone points.

3. Combining the macro and micro characteristics of the backbone, a visual crack width measurement method that is closer to the actual needs of the project is used to obtain a more accurate measurement method.

4. Two evaluation measurement standards (i.e., recall rate and direction error) are added to enable a more comprehensive evaluation of the measurement method.

The remainder of this article is structured as follows. The process and principle of the crack width measurement method are described in Section 2. Section 3 presents the relevant evaluation test conducted on the proposed method. Section 4 provides concluding remarks and outlines possible future study.

2 Methods

2.1 Visual crack-measurement process

The basic processes of the width-measurement method proposed in this study include crack segmentation, backbone refining, and width measurement. The specific process is shown in Fig. 1. Previous studies have shown that the U-Net semantic segmentation model is sensitive to edge detail features, which also suggests that it would be suitable for dam-crack segmentation [49–52]. In this article, the input into U-Net was an RGB image and the output is a semantically segmented binary image. The process of semantic segmentation takes place in a code-decoded symmetrical U-shaped structural model, hence the name U-Net. The acquisition of the parameters in the U-shaped structural model requires convolutional inference of a large number of labeled samples, the result of which is then recorded in the model file. When using U-Net, this model file is called and the image data is passed into the model. The segmentation result can be obtained after calculation by U-Net, which is a very simple and commonly used semantic segmentation model. In this study, the results of the U-Net semantic segmentation model were therefore directly used as the input material for the pretreatment of the crack backbone extraction and crack width measurement. Pretreatment can effectively handle possible misjudgment problems in crack segmentation while improving the robustness of backbone refining. Morphology (large) represents the morphological processing of the large window, which is used for the segmentation of the crack area; morphology (small) represents small window morphology processing, which is used to strengthen the connectivity of the crack binary image. Morphological processing here referes to dilation or erosion algorithms (they have opposite effects to each other), whose role is to expand the binarized target towards the background. Combinatorial binarization is the combined operation of binarization–blur–binarization, which is used to smooth the crack binary image and eliminate segmentation impurities before backbone extraction. The role of blur is also to expand the target, but its effect is more moderate than that of morphological processing.

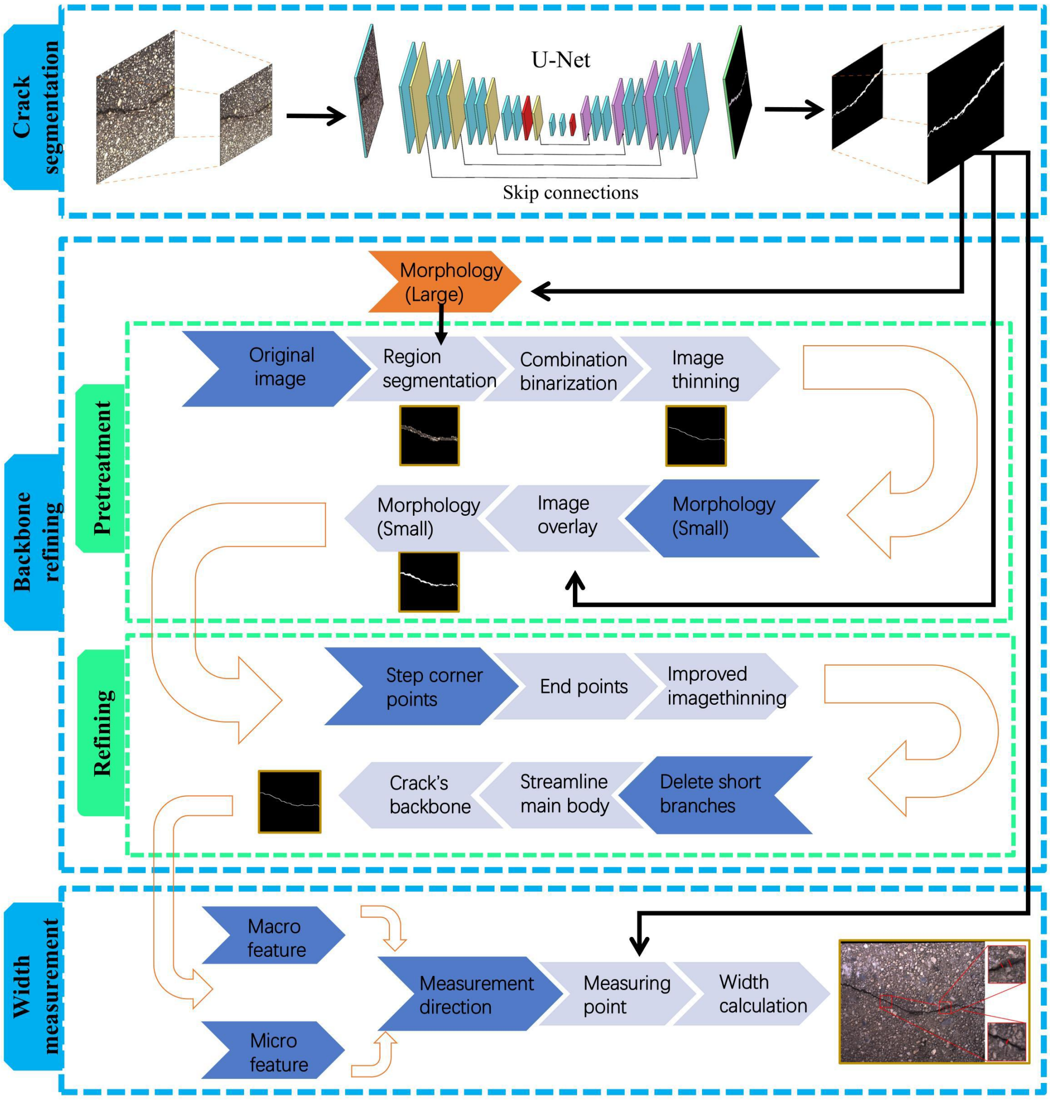

Fig. 1 Framework and flowchart for visual measurement

2.2 Crack backbone refinement

To address the problem of redundant data points when the image-refinement algorithm extracts the crack skeleton, we refine the crack skeleton and the backbone of the crack using the improved image-refinement algorithm to mark the ends of the cracks while avoiding end-shortening during refinement. The refinement of the crack backbone removes redundant points on the branches and backbones based on the skeleton.

The backbone of the crack contains information on the shape of the crack, which has the function of determining its position and providing the basis for measuring its width. The classic Zhang–Suen image thinning algorithm [53] can be used to extract the crack skeleton, but the skeleton still has redundant data, which can be further streamlined to obtain the backbone of the crack. For the convenience of comparison and explanation in this work, it is stipulated that the output of the Zhang-Suen image thinning algorithm is called "skeleton", and the output proposed for improvement and further processing based on the Zhang-Suen image thinning algorithm is called "backbone".

The input into the crack backbone refinement algorithm is a crack binary image with only crack and background pixels. This process involves iterative refinement. In each iteration, the outermost contour is transformed into the background. The algorithm sets a certain crack pixel as $P0$. Starting from the pixel just above $P0$, the eight neighborhoods of $P0$ are set as $P1$ to $P8$, clockwise. The background point is assigned a value of either zero or one, as shown in Fig. 2.

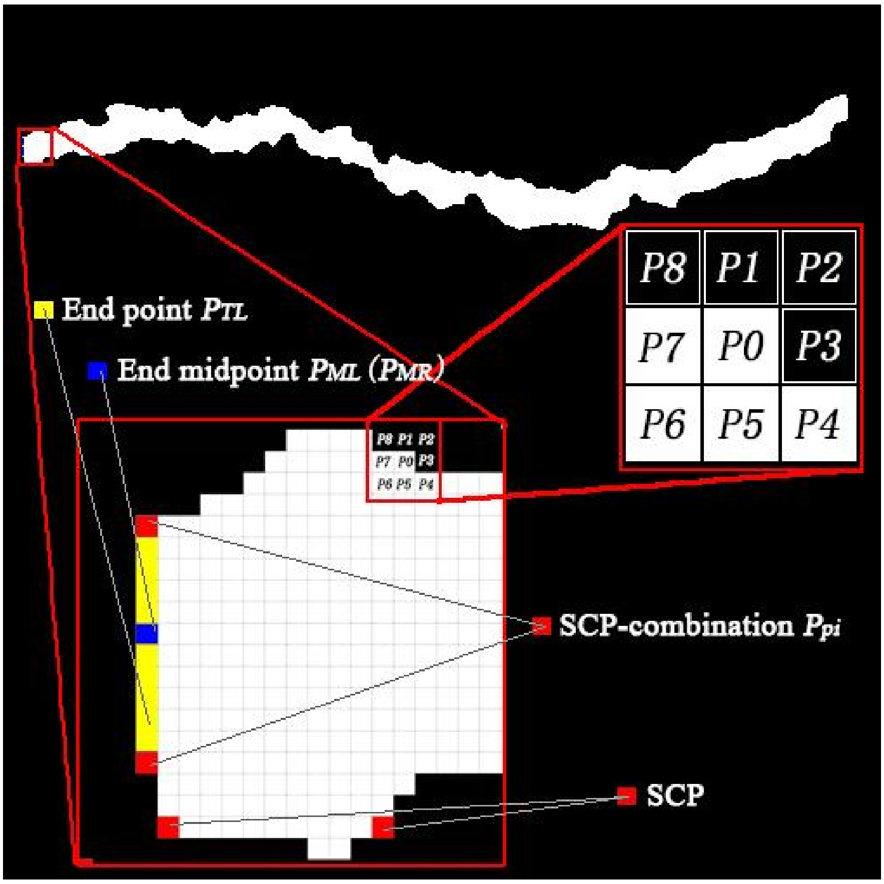

Fig. 2 Feature points in crack binary graph

Detecting the edge of the crack binary image involves multiple steps. As shown in Fig. 2, each step with a vertex height greater than 1 pixel is the step corner point (SCP), which can be found according to its eight-neighborhood features and is used to build set CoP . Let $P_0(\Delta P)$ denote the set of P_0's eight neighborhoods satisfying condition ΔP . The set, CoP , is given by the formula $CoP = \left\{P_0 \middle| P_0\left(\Delta P\right)\right\}$, in which ΔP is defined by Eq. (1):

$$\begin{aligned}&\exists\left(P_1+P_2+P_3=3\wedge P_5+P_6+P_7+P_8=0\right)\\&\vee\left(P_3+P_4+P_5=3\wedge P_1+P_6+P_7+P_8=0\right)\\&\vee\left(P_5+P_6+P_7=3\wedge P_1+P_2+P_3+P_4=0\right)\\&\vee\left(P_7+P_8+P_1=3\wedge P_2+P_3+P_4+P_5=0\right),\quad P_0\in P_0\left(\Delta P\right)\end{aligned}, \tag{1}$$

In CoP , the two SCPs in the same column are recorded as a set, P_{pi} , and its midpoint, P_{piM} , is marked from there, as shown in Fig. 2. Then, according to the eight-neighborhood feature, the P_{piM} in the left and right ends of the crack, which are regarded as P_{ML} and P_{MR} , can be separated from the set of all P_{piM} . P_{ML} and P_{MR}'s eight neighborhoods at the left and right ends to satisfy Eq. (2).

$$\begin{aligned}&(a)P_6+P_7+P_8=0\Rightarrow P_{ML}\\&(b)P_2+P_3+P_4=0\Rightarrow P_{MR}\end{aligned}, \tag{2}$$

The pixels in the same column as P_{ML} or P_{MR} are the crack's end points—recorded as P_{TL} and P_{TR} , respectively. If P_{TL} and P_{TR}'s eight neighborhoods satisfy the condition $P_1+P_5=2$, they are respectively recorded in sets $TePL$ and $TePR$. The purpose of this move is to eliminate the points overlapping the edges among the endpoints during the refinement process.

Let $A(P_0)$ denote the number of 01 patterns of the clockwise connections in the eight neighborhoods of P_0 and $B(P_0)$ denote the number of crack pixels in the eight neighborhoods of P_0 . One iteration of the crack backbone extraction algorithm is divided into odd- and even-numbered sub-iterations. In each sub-iteration, the crack pixels that satisfy Eq. (3) are marked as the outermost pixels, which are uniformly converted into background pixels before the iteration completes. In even-numbered sub-iterations, only conditions (c), (d), and (e) are respectively changed to (c’), (d’), and (e’).

$$\begin{aligned}
&(a)\,A(P_0)=1\\
&(b)\,2\le B(P_0)\le 6\\
&(c)\,P_1\times P_3\times P_5=0\\
&(d)\,P_3\times P_5\times P_7=0\\
&(e)\,P_0\notin TePR\\
&(c')\,P_1\times P_3\times P_7=0\\
&(d')\,P_1\times P_5\times P_7=0\\
&(e')\,P_0\notin TePL
\end{aligned}, \tag{3}$$

The algorithm iteratively thins the cracks to obtain the skeleton according to the above rules until no crack pixels are marked as outermost pixels. However, there are still numerous redundant points in the skeleton that can be streamlined further. The streamlining process is divided into two steps: deleting short branches and streamlining the skeleton’s main body to obtain the backbone.

To delete short branches, the skeleton’s endpoints are marked on the left and right sides of the image and other endpoints satisfying $B(P_0)<2$, or $B(P_0)=2$ and $A(P_0)=1$, apart from the skeleton’s endpoints. Once an end point is deleted on the short branch, the connected point becomes the new endpoint. These operations are repeated several times until all short branches are deleted. The deletion process is illustrated in Fig. 3.

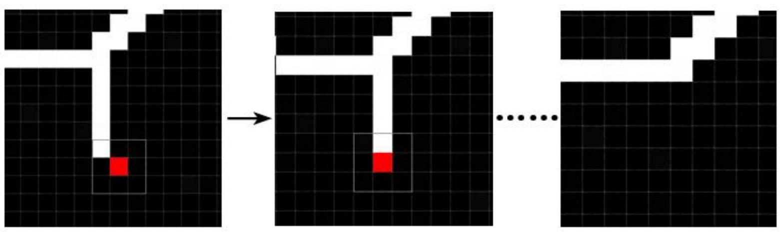

Fig. 3 Short branch deletion process

The refinement of the backbone is to convert pixels in the skeleton line that satisfy any of the items in Eq.(4) to the background. If the image is scanned from the first pixel in the upper left corner to the last pixel in the lower right corner, then, as shown in Fig. 4, the red pixels are deleted. After cleaning, the backbone is obtained with the following features:

(1) The total number of backbone pixels in each point's eight-neighborhood does not exceed 2.

(2) Its eight-neighborhood pixel distribution will show four shapes: v shape, linear shape, semi-Y shape of left and semi-Y shape of right. Plus, when each shape is rotated around the center, the number of neighborhood distribution types of backbone points is reduced to $C_4^2 + C_2^1 + C_4^1 C_2^1 = 16$, as shown in the lower right corner of Fig. 4.

$$\begin{aligned} &(a) P_1 + P_3 = 2 \\ &(b) P_1 + P_7 = 2 \\ &(c) P_5 + P_3 = 2 \\ &(d) P_5 + P_7 = 2 \end{aligned}, \tag{4}$$

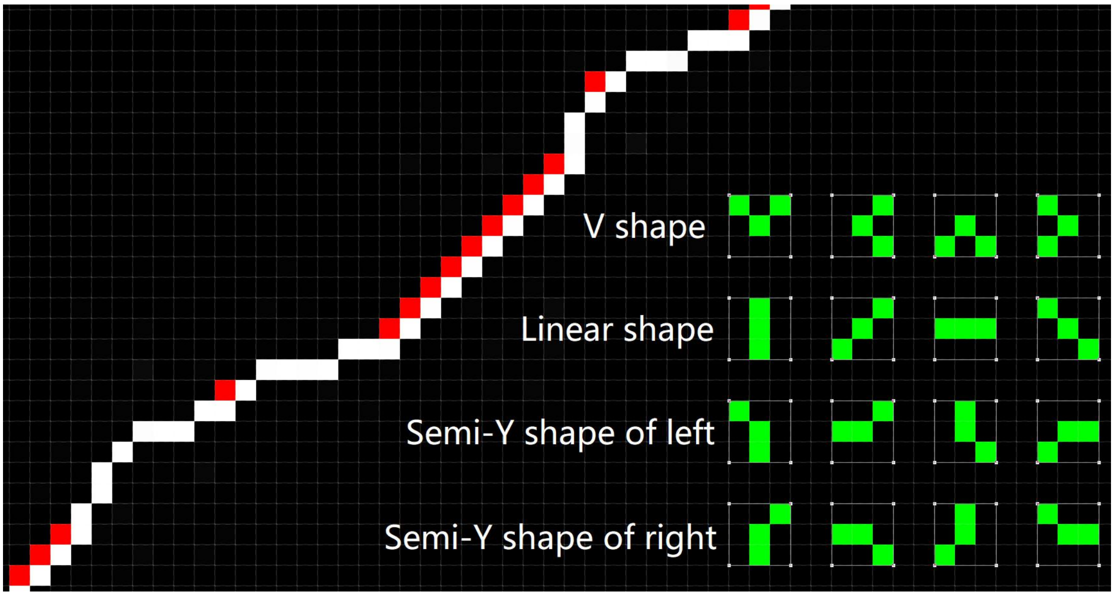

Fig. 4 Streamlined backbone

Fig. 5 illustrates the effect of the main crack extraction. The backbone extraction algorithm in this paper is more streamlined than others. In total, compared with the classic Zhang-Suen image thinning algorithm, the crack backbone refinement algorithm in this paper has the following characteristics:

1. The branches are removed and the shape of the end of the crack is retained (as shown in the upper left corner of Fig. 5a and upper right corner of Fig. 5b);

2. The eight-neighborhood effective pixels of the backbone do not exceed 2 and there are

only 16 types of neighborhood pixel distribution (as shown in the lower right corner of Fig. 4 and the lower right corner of Fig. 5).

While simplifying the amount of data, it is convenient to use the neighborhood distribution type to classify the backbone points, which is conducive to the subsequent clear definition of the crack-width measurement.

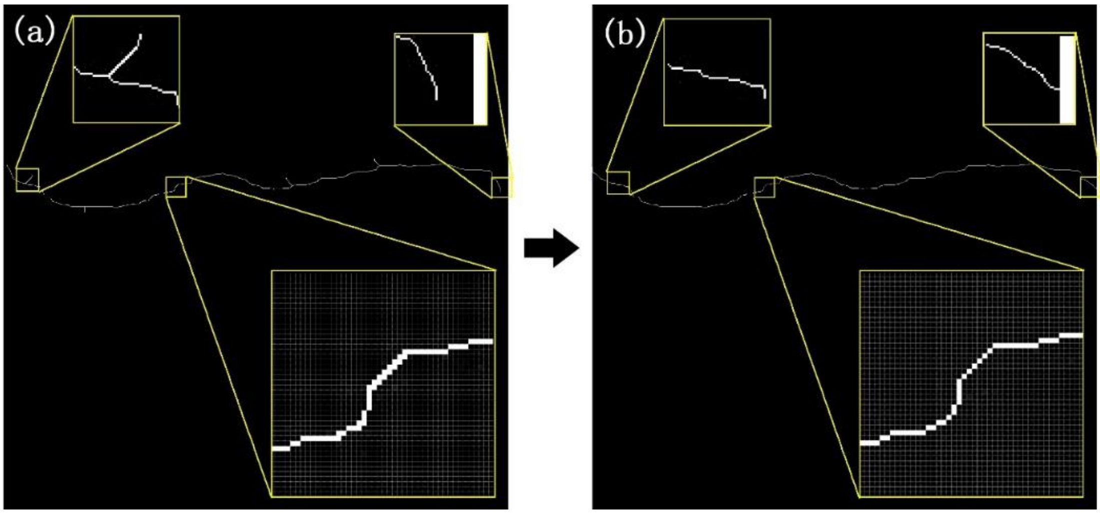

Fig. 5 Classic thinning algorithm (a) compared with the improved backbone refining algorithm in this study (b)

2.3 Determining the crack width measurement direction

As shown in Fig. 6, there are multiple measurement schemes that rely on the same measurement position, O. The measurement schemes AE, BF, CG and DH are the width-measurement results obtained at position O in different measurement directions. Notably, they are quite different from each other. The width is measured along the normal direction of the crack-growth direction according to the visual inspection method commonly used by engineers in practice. Evidently, the solution BF is more suitable for characterizing the width of the crack at position O. The main objective of this section is to get as many measurement points as possible and determine the width of the crack in the visual measurement along the optimum measurement direction to closely approximate the width obtained by the commonly used method in practice.

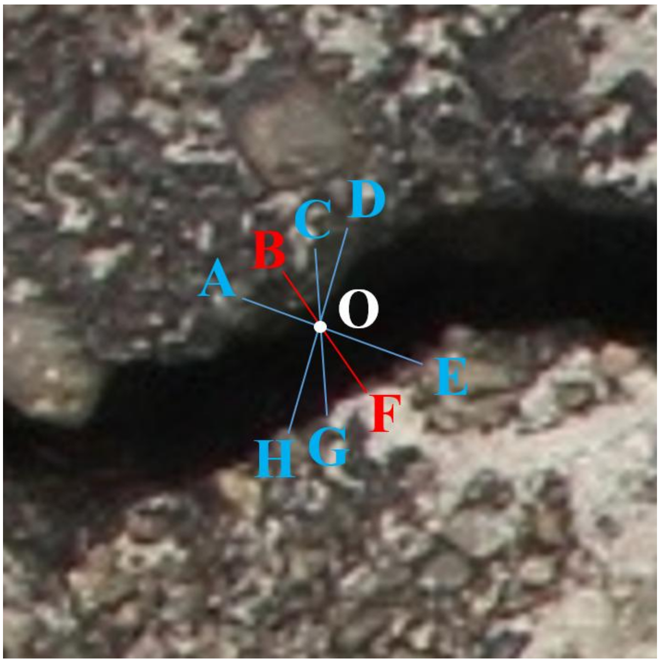

Fig. 6 Different measurement methods on the same crack

This paper proposes a method for determining the direction of crack width measurement based on the dual-scale features of the backbone. The proposed method combines the slope information of the crack backbone at the macroscale with its neighborhood information at the microscale. The macroscale information is based on the trend of the entire backbone of the crack, whereas the microscale information is based on the neighborhood distribution information of each pixel of the crack backbone. The combined method defines eight measurement directions, and then macro- and micro-scale information is matched to each of these eight directions. When the dual-scale information matches, the measurement direction can be determined and obtained. For points where the macroscale and microscale information do not match, the measurement is abandoned. Because the point where the direction is incorrect or cannot be measured will affect the reliability of the measurement result.

At the macro level, this study uses the least-squares method to fit the n-degree polynomial curve of the main stem into a polynomial function, $v = f(u)$, as established in Eq. (5):

$$\begin{bmatrix} v_1 \\ v_2 \\ \vdots \\ v_m \end{bmatrix} = \begin{bmatrix} 1 & u_1 & \cdots & u_1^n \\ 1 & u_2 & \cdots & u_2^n \\ \vdots & \vdots & \ddots & \vdots \\ 1 & u_m & \cdots & u_m^n \end{bmatrix} \times \begin{bmatrix} w_1 \\ w_2 \\ \vdots \\ w_n \end{bmatrix}$$
$$\boldsymbol{V} = \boldsymbol{U} \times \boldsymbol{W} \tag{5}$$

where (u_m, v_m) is the coordinate value of the backbone point in the image coordinate system, W is the coefficient matrix of the polynomial function, m is the number of backbone points participating in the polynomial curve-fitting, n is the order of the highest degree of the curve, and $n=9$.

The least-squares method is used to solve matrix W, as shown in Eq. (6):

$$\boldsymbol{W} = \left(\boldsymbol{U}^T\boldsymbol{U}\right)^{-1}\boldsymbol{U}^T\boldsymbol{V}. \tag{6}$$

The first-order derivative of the function can be used to obtain the slope, dv_m, at any point on the backbone, as shown in Eq. (7):

$$dv_m = \sum_{i=1}^{n} a_{n-i} u_m^{n-i-1}. \tag{7}$$

The angle, θ, between a straight line passing through any backbone point and the horizontal axis represents the measurement direction. This study defines eight measurement directions with an interval of 22.5° between each. At the macro level, mapping is defined from the slope, dv_m, of the curve, $v=f(u)$, to the macro measurement direction, ϕ, as shown in Eq. (8).

$$\phi = \begin{cases} 0°, dv_m \in (-\infty, \tan 101.25°) \cup [\tan 78.75°, +\infty) \\ 22.5°, dv_m \in [\tan 101.25°, \tan 123.75°) \\ 45°, dv_m \in [\tan 123.75°, \tan 146.25°) \\ 67.5°, dv_m \in [\tan 146.25°, \tan 168.75°) \\ 90°, dv_m \in [\tan\text{-}11.25°, \tan 11.25°) \\ 112.5°, dv_m \in [\tan 11.25°, \tan 33.75°) \\ 135°, dv_m \in [\tan 33.75°, \tan 56.25°) \\ 157.5°, dv_m \in [\tan 56.25°, \tan 78.75°) \end{cases}. \tag{8}$$

At the microscale, there are only 16 types of eight-neighborhood distributions of backbone points, and the number is relatively small. The mapping from the backbone point to the microscale measurement direction, φ , can be defined according to the eight-neighbor distribution types, as shown in Eq. (9).

$$\varphi = \begin{cases} 0°,(p1+p5=2)\vee(p6+p8=2)\vee(p2+p4=2) \\ 22.5°,(p1+p4=2)\vee(p5+p8=2)\vee(p1+p5=2) \\ 45°,(p4+p8=2)\vee(p1+p4=2)\vee(p5+p8=2) \\ 67.5°,(p4+p7=2)\vee(p3+p8=2)\vee(p3+p7=2) \\ 90°,(p3+p7=2)\vee(p4+p6=2)\vee(p2+p8=2) \\ 112.5°,(p2+p7)=2)\vee(p3+p6=2)\vee(p3+p7=2) \\ 135°,(p2+p6=2)\vee(p1+p6=2)\vee(p2+p5=2) \\ 157.5°,(p1+p6=2)\vee(p2+p5=2)\vee(p1+p5=2) \end{cases} . \tag{9}$$

In fact, using only the macro- or micro-scale information of the backbone for direction determination may cause a large direction error. On the one hand, the polynomial curve fitted at the macroscale is continuous and smooth, and it is difficult to accurately fit the growth morphology of the crack backbone, as shown in Fig. 7; the white dots constitute the crack's backbone and the orange line is the smooth curve after fitting. They do not exactly coincide. On the other hand, at the microscale, as shown in the lower left corner of Fig. 4, only three pixels are used as the basis for direction determination at a time, which is insufficient to express the current growth state of the crack. In the blue circle in Fig. 7, manual measurement should be carried out in the 45° direction. However, as shown in the red circle, if microscale information has been used for measurements, it is measured in the vertical direction. Similarly, in the green circle, the vertical direction should be followed when taking the manual measurement. However, as shown in the yellow circle, if macroscale information has been used, it is still measured in the 45° direction.

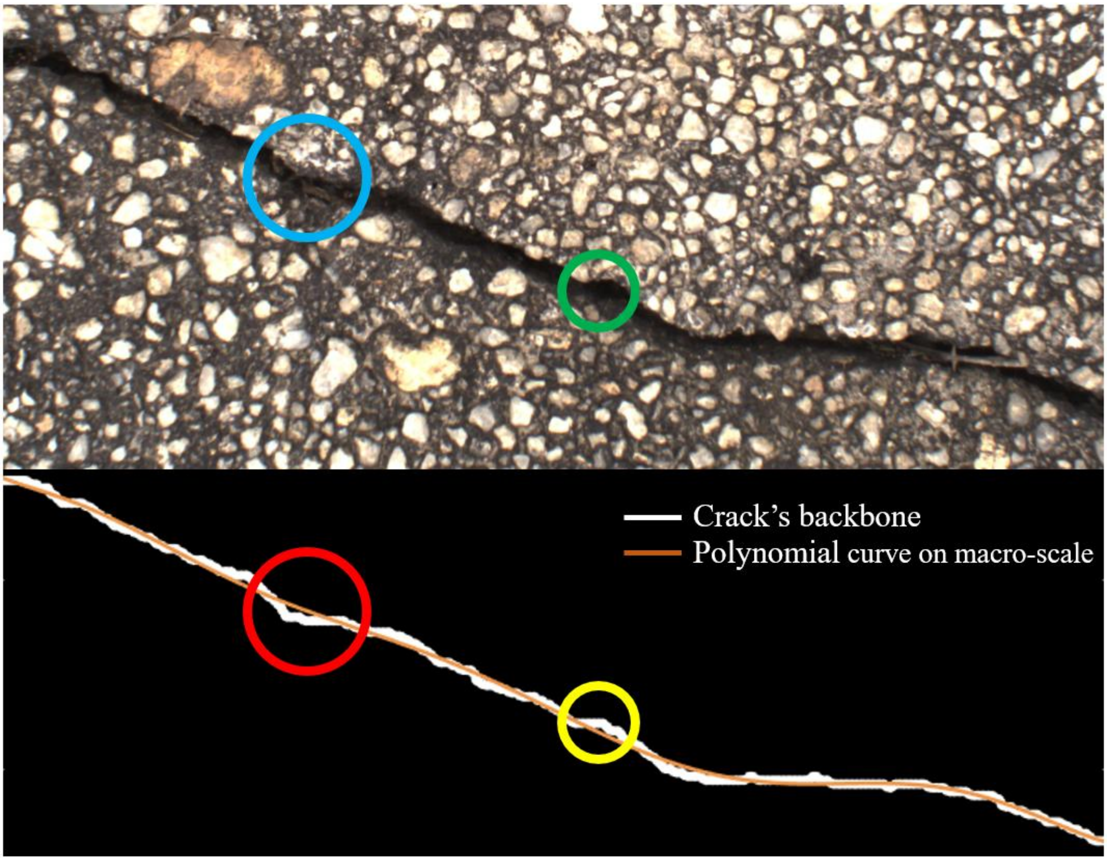

Fig. 7 Polynomial curve vs crack's backbone

Therefore, the measurement direction determination method must be designed to avoid errors in direction determination when using macroscopic or microscopic scale information alone. When solving the microscale direction, φ, this method is a situation where there are multiple neighborhood distribution types corresponding to one direction. Therefore, the microscale direction φ can be seen as a constraint on the macroscale direction, ϕ. When the macroscale, ϕ, and microscale, φ, directions of the backbone point are equal, the measurement direction, θ, of the point can be expressed as $\theta = \phi = \varphi$.

2.4 Crack width measurement

The straight line measurement, L_m, is defined according to the measurement direction and the main point, and the crack point (u_i, v_i) closest to L_m is found to form a point set, P_d, as in

Eq. (10):

$$P_d = \{(u_i, v_i) \mid |v_i - (\tan\theta * u_i + b)| < 1\}, \tag{10}$$

where b is the intercept of the linear equation, which can be obtained by substituting the coordinates of the backbone point into the equation.

The set P_d includes the upper edge measurement point, P_{mu}, and the lower edge measurement point, P_{md}, of the crack. As shown in Fig. 8, the yellow dots indicate the crack's backbone, the red dot is the measurement position at that place, the blue dots are P_d, and the green pixels are the two measurement points found according to the above method.

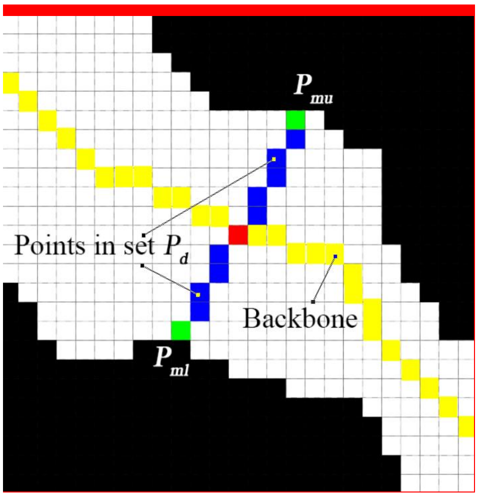

Fig. 8 Acquisition process for the measuring points

The values of P_{mu} and P_{ml} are shown in Eqs. (11) and (12):

$$P_{mu}\begin{cases}(u_{\max}, v_{\min}), 0° \le \theta < 90° \\ (u_{\min}, v_{\min}), 90° \le \theta < 180°\end{cases}, \tag{11}$$

$$P_{ml}\begin{cases}(u_{\min}, v_{\max}), 0° \le \theta < 90° \\ (u_{\max}, v_{\max}), 90° \le \theta < 180°\end{cases}. \tag{12}$$

As shown in Fig. 9, the blue line indicates the measurement method of the proposed method at this location, and the cracks covered by the blue lines can represent the range that can be measured on the crack image of this scheme.

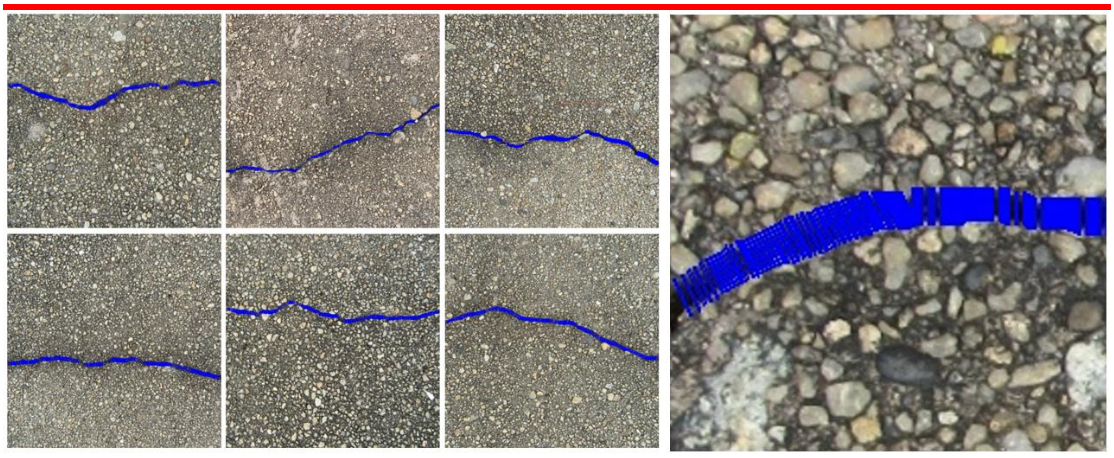

Fig. 9 Measurable point of a section of a crack and its measurement scheme

In this study, a binocular vision system is used for width-vision measurement, and the camera's sight axis is set perpendicular to the dam surface. Before measurement, the camera must be double-targeted to correct distortion and to perform epipolar line correction between the two cameras. Template matching is used to obtain four 50×50 image blocks on the right image corresponding to the upper-left, lower-left, upper-right, and lower-right of the left image. A four-dimensional vector, $\boldsymbol{uB}_i=[u_{Li} \quad v_{Li} \quad u_{Li}-u_{Ri} \quad 1]^T$, is constructed for the center of each image block $(u_{Li}, v_{Li})^T$, representing the coordinates of the center point of the image block on the left image in the image coordinate system. u_{Li}-u_{Ri} represents the disparity value, d, of the center point of the same image block on the left and right images. The triangulation principle, $\boldsymbol{CB}=\boldsymbol{Q}\times\boldsymbol{uB}$, is used to obtain the coordinates, $\boldsymbol{CB}_i=(X_{Ci}, \ Y_{Ci}, \ Z_{Ci}, \ W_i)^T$, of the centers of the four image blocks in the camera coordinate system. $\boldsymbol{Q}$ is the reprojection matrix, which is obtained by the camera's dual objective setting, and $\boldsymbol{W}$ is a constant. The average of the four depth values indicates the average depth of the camera's optical center from the dam surface. Equation (13) is used to calculate the crack width, W_c, represented by the two measurement points, $P_{mu}(u_{mu}, v_{mu})$ and $P_{md}(u_{md}, v_{md})$.

$$W_c=\frac{\overline{Z}}{f_x \cdot f_y}\sqrt{f_y^2 \cdot (u_{mu}-u_{md})^2 + f_x^2 \cdot \pi (v_{mu}-v_{md})^2} \ . \tag{13}$$

Between these, f_x and f_y are the internal parameters of the camera, which represent the product of the physical focal length of the lens and the size of each unit in the x and y directions of the imaging device, respectively, which are obtained by camera calibration.

3 Test results and analysis

The test site of this study was Fenghuang Reservoir Dam in Conghua District, Guangzhou City, Guangdong Province. The dam of this reservoir has obvious cracks, and the samples are abundant. The test site is shown in Fig. 10.

For the crack backbone extraction algorithm, we set the reduction rate test to illustrate the performance of the algorithm when reducing the amount of data. To measure the performance of the direction determination method, we used the two evaluation criteria proposed in this study: the recall rate of the direction determination and the direction error, and the corresponding judgment method. A segmentation performance evaluation test and a width-vision measurement accuracy test were conducted. For the ground truth, we referred to the experiment in Section 4.2 of [26]. Six researchers marked the cracks; the direction of the crack width was the tangent direction of the commonly used crack growth, and the width was the distance between two points on the edge of the crack in the measurement direction.

Fig. 10 Test equipment and environment

3.1 Segmentation performance evaluation

A total of 5,760 sample images were used for training, all samples were randomly arranged, and the training, validation, and test sets were randomly allocated at a ratio of 6:2:2. For the training input and prediction output of the model, a square image with a resolution of 400 × 400 pixels was used. The Adam optimization algorithm was used in all relevant procedures.

For the trained U-Net model, commonly used semantic segmentation evaluation indicators were used (i.e., pixel accuracy [PA], average pixel accuracy [MPA], average intersection and combination ratio [MioU], and frequency weight intersection and combination ratio [FWIoU]) to evaluate the performance of U-Net segmentation for dam-crack evaluation. The evaluation was based on a test set having 1,152 images of dam cracks. The segmentation results of the model were decomposed to the original size of the test images via linear interpolation.

To evaluate the segmentation effect of U-Net, the crack segmentation effects of the common semantic segmentation networks, SegNet and DeeplabV3+ (with Xception and MobileNetv2 as the backbone networks, respectively), were added for comparison. The distributions of their performance evaluation scores are shown in Fig. 11, while visual comparisons are presented in Fig. 12. The abscissa is the order of the graph, and the ordinate is the score.

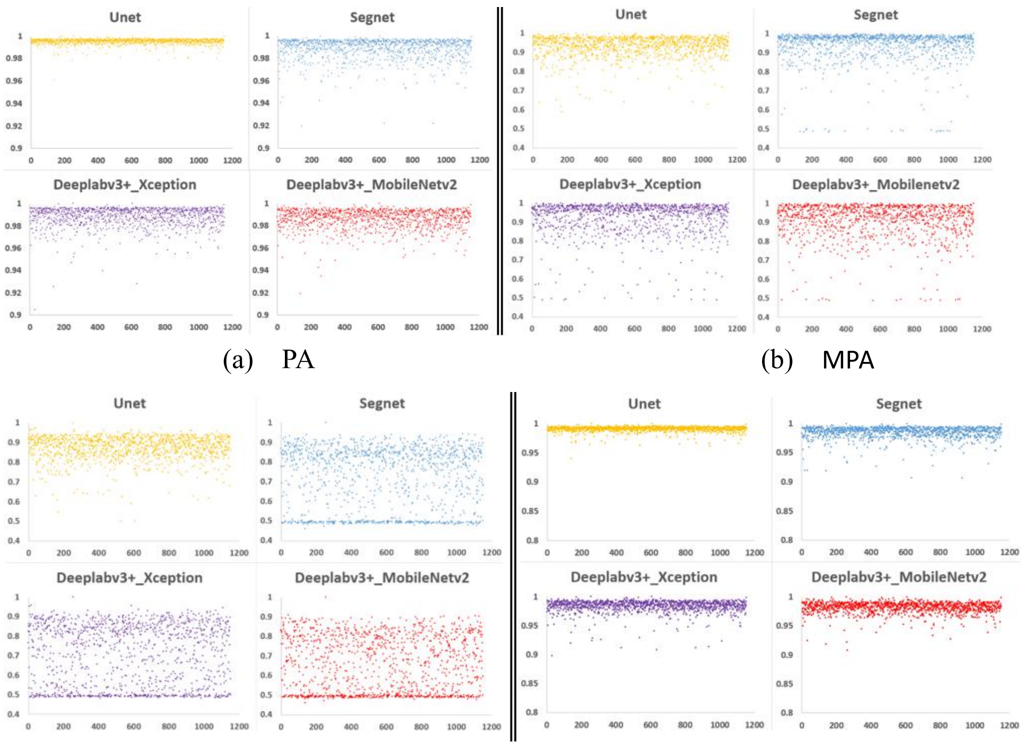

(a) PA (b) MPA

(c) MIoU (d) FWIoU

Fig. 11 Distribution comparison of the crack segmentation performance scores

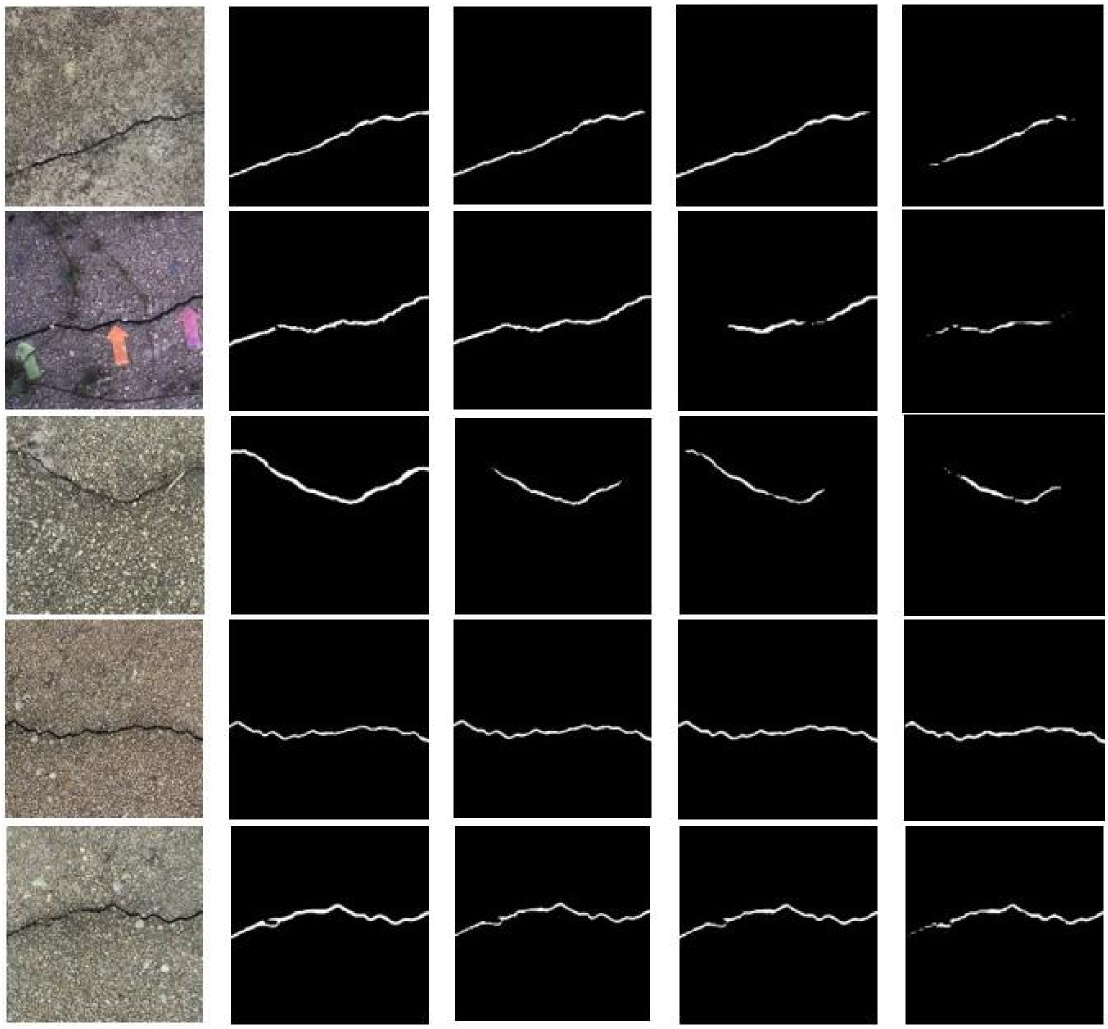

(a) Source (b) U-Net (c) SegNet (d) D+X (e) D+M

Fig. 12 Visual comparison of segmentation effects

The statistical results of the average and standard deviations of the performance evaluation scores are shown in Table 1.

Table 1. Statistics of the average and standard deviation of U-net performance evaluation scores

	PA		MPA		MIoU		FWIoU	
	Average	S.D.	Average	S.D.	Average	S.D.	Average	S.D.
U-Net	99.5 %	0.003	93.1 %	0.054	87.1 %	0.062	99.1 %	0.005
SegNet	98.9%	0.009	93.5%	0.084	72.5%	0.153	98.5%	0.010
D+X	98.8%	0.009	92.1%	0.087	70.8%	0.154	98.4%	0.011
D+M	98.6%	0.009	91.1%	0.089	65.8%	0.139	98.2%	0.010

* D+X is Deeplabv3+ with the backbone network of Xception, while D+X is MobileNetv2.

The results show that U-Net has higher segmentation accuracy and stability in the task of segmenting dam cracks than the other networks. Thus, a better improvement plan based on U-Net would be worthwhile. Consequently, U-Net segmentation results were directly used for subsequent width measurement in this study.

3.2 Evaluation of streamlining performance of crack backbone extraction algorithm

In this section, we compare the total number of backbone points (S_B , obtained by applying the backbone extraction algorithm) and the total number of skeleton points (S_S , obtained by applying the Zhang–Suen image-refinement algorithm) on the same crack segment to measure the streamlining performance of the crack backbone extraction algorithm proposed in this paper. The simplification rate of the crack backbone extraction algorithm relative to the Zhang–Suen image-refinement algorithm is R_e:

$$R_e = \frac{S_S - S_B}{S_S} \times 100\% . \tag{14}$$

Taking 100 randomly selected crack images as the samples in the experiment, the statistics of the results obtained are as shown in Fig. 13 and Table 2.

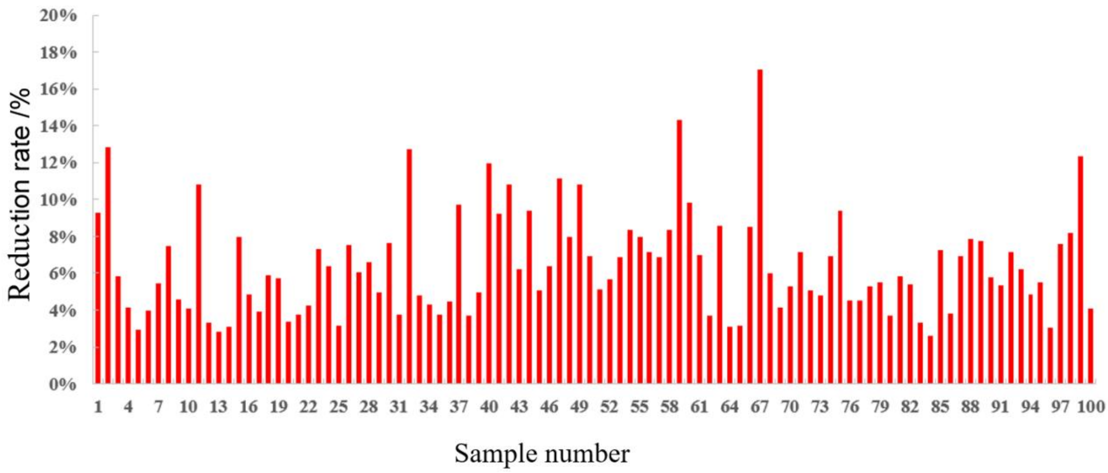

Fig. 13 Reduction rate test results

Table 2. Statistical results of the reduction rate test

	Mean	Median	Max	Min	S.D.
Reduction rate	6.40 %	5.82 %	17.04 %	2.60 %	3 %

As shown in Fig. 13 and Table 2, the skeleton obtained by the crack backbone extraction algorithm had an average simplification rate of 6.40 % compared with the skeleton obtained using the Zhang–Suen image-refinement algorithm. On the one hand, it showed that the skeleton obtained by the Zhang-Suen image thinning algorithm was universally spaced for further optimization. On the other hand, the measurement direction determination method in this paper was related to the eight-neighborhood pixel distribution of the backbone points, and the streamlining of the skeleton was conducive to the improvement of the matching degree of the macro- and micro-scale measurement direction information of the backbone. Thus, the streamlining performance was good. In addition, it is worth emphasizing that the crack backbone extraction algorithm proposed in this study had no more than two neighboring points for each backbone point, greatly reducing the number of backbone point neighborhood distribution types to only 16, which was convenient for classifying backbone points according to neighborhood distribution types.

3.3 Recall rate of direction determination method

The recall rate of the direction determination method refers to the ratio of the total length of each segment of cracks that can be visually measured in the width to the total length of the cracks in the image, which is used to investigate the recall performance of the measurement algorithm on the task of crack width measurement. On the other hand, the recall rate can also reflect the matching degree between the macro- and micro-scale information of the crack's backbone in the measurement direction determination problem in this method, because the backbone points of the macro- and micro-scale mismatch were the negative sample in the recall statistics. Number of pixels was used to approximate the length of the crack section. Using the direction determination method proposed in this study, the total number of measurable points, P_C, was obtained, and the total number of crack main points, P_S, was counted. The recall rate, R, is given by Eq. (15):

$$R = \frac{P_C}{P_S} \times 100\% . \tag{15}$$

In this study, 100 samples were randomly selected on the test set of U-Net crack segmentation, and the segmentation results were used as samples for the recall test. In addition, the control group used the same crack sample set, but the input of direction determination was the skeleton obtained by the Zhang–Suen thinning algorithm [53]. This was done to demonstrate the advantages of the proposed backbone extraction algorithm in the direction determination recall. The recall test results are shown in Fig. 14, where the red label represents the proposed method and the blue label represents the control group. The statistical results are listed in Table 3, where the label “Improved” represents the proposed method. The results show that the average recall rate of the proposed width-measurement direction determination method is approximately 74.90 %, and a standard deviation of 4 % indicated that the measurement was stable. They all outperformed the control group; the full-search performance was good overall. At the same time, the results show that the macro and micro information of the backbone points in the measurement direction determination problem were well matched, so that averaging three-quarters of the crack sections can make a more accurate measurement. More accurate here means that measurements with directions as a guide were theoretically more accurate than the measurement method which did not distinguish between measurement directions.

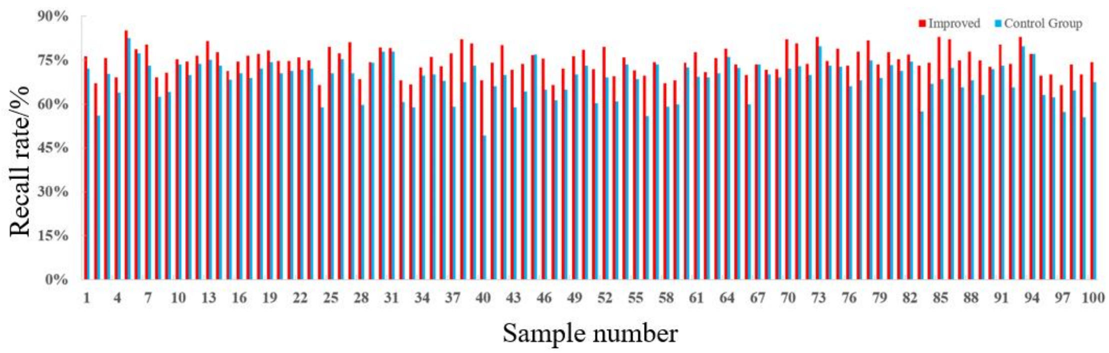

Fig. 14 Recall rate of the proposed width-measurement direction determination method

Table 3 Statistical results of the recall rate of the proposed direction determination method

	Mean	Median	Max	Min	S.D.
Improved	74.90%	74.73%	85.01%	66.36%	4%
Control Group	68.53%	69.82%	82.52%	49.24%	6%

3.4 Orientation error of width measurement direction determination

The direction error was used to evaluate the accuracy of the direction. We randomly selected 10 backbone points, P_{mi}, from the measurable points, and their positions were recorded and marked on the image. We invited three technicians to determine the measurement direction of the crack at the position marked on the image based on their experience, taking the tangential direction of the crack-growth direction as the measurement direction. Hence, pixel points A and B were selected on the two edges of the crack, and the mark point, P_m, had to be on the line section AB or as close to it as possible.

The width measurement direction determination method was used to determine the measurement direction of the mark point, P_{mi}, and the crack-edge points, C and D, were recorded in this direction. We composed vectors $\overrightarrow{AB}$ and $\overrightarrow{CD}$ to find the acute angle between them. $\Delta\theta$ represents the determination error of the measurement direction, as shown in Eq. (16).

$$\Delta\theta = \arccos\left(\frac{\overrightarrow{AB}\bullet\overrightarrow{CD}}{|\overrightarrow{AB}|\bullet|\overrightarrow{CD}|}\right). \tag{16}$$

From 30 sample images, 10 points were randomly selected for testing and compared with the method proposed by Luo et al. [46]. Fig. 15 shows the distribution of the test results.

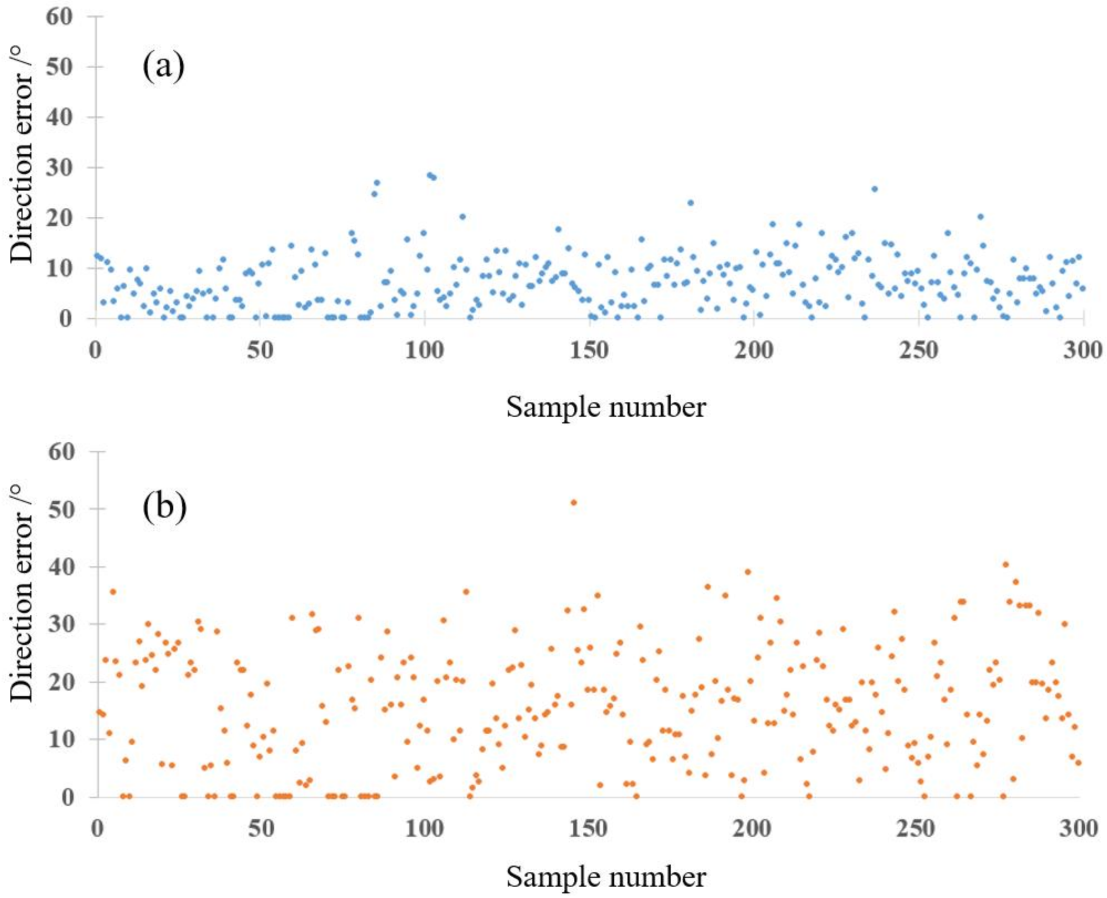

Fig. 15. Distribution of direction errors of width measurement direction determination methods: (a) proposed method; (b) method proposed by Luo et al. [46]

The statistical average, median, maximum, minimum, and standard deviation values are listed in Table 4.

Table 4. Direction error statistics of width measurement direction determination methods

	Mean /°	Median /°	Max /°	Mini /°	S.D. /°
Proposed method	6.97	6.45	28.10	0	5.39
Method proposed by Luo et al.[46]	15.44	15.09	51.01	0	10.25

The direction error of the proposed direction determination method was 6.97°, the median was 6.45°, the standard deviation was 5.39°, and the direction error did not exceed 28.10°, which is significantly better than the method by Luo et al. [46]. The above experiments show that the proposed method to determine the width measurement direction has practical accuracy and stability.

3.5 Test platform accuracy

The spatial distance between the two corner points of the calibration board was calculated by visual measurement and compared with the actual distance, which can be used to reflect the measurement accuracy of the test platform in this study. The calibration board was placed on the dam so that both the left and right cameras could shoot all corners while maintaining the state to continuously collect 200 images of the calibration board at 2 s intervals, correct them, and select 12 diagonal points on the board as sample points, as shown in Fig. 16.

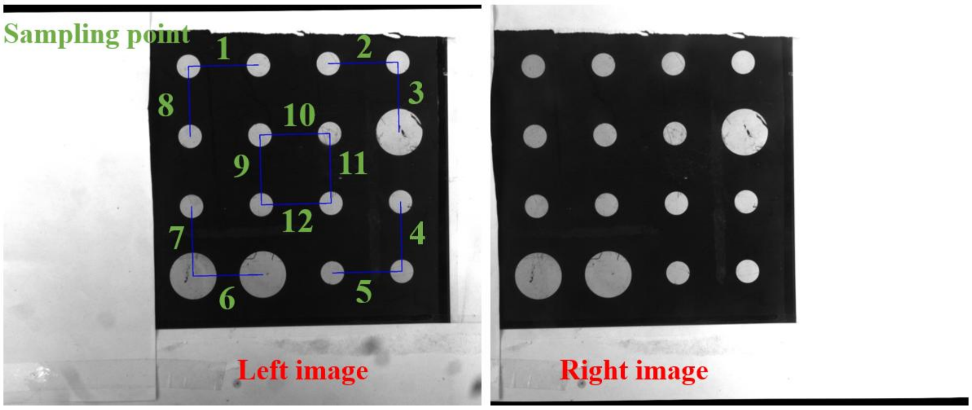

Fig. 16 Left and right images of the calibration board at the test site

The error between the visual distance measurement and the actual distance of each sampling point was used to determine the systematic error of the test device. In the experiment, the average ($\overline{\mu_B}$) and standard deviation (σ_B) of the error data, maximum absolute error (m_B) , average distance (R_B) from all repeated sampling points to the mean, and distance (D_B) between the maximum and minimum error data were used to evaluate the test device system error conditions. The results are presented in Table 5.

Table 5. Statistical value of the system error of the test device in this study

Serial number	$\overline{\mu_B}$	m_B	σ_B	R_B	D_B
Sampling point 1	0.007	0.035	0.011	-0.001	0.101
Sampling point 2	0.006	0.035	0.010	0.006	0.058
Sampling point 3	-0.001	0.024	0.010	-0.001	0.076

Sampling point 4	0.016	0.055	0.009	0.016	0.067
Sampling point 5	0.016	0.052	0.008	0.012	0.059
Sampling point 6	0.058	0.112	0.011	0.057	0.088
Sampling point 7	-0.004	0.0489	0.013	-0.004	0.082
Sampling point 8	0.006	0.044	0.013	-0.013	0.130
Sampling point 9	-0.033	-0.002	0.007	-0.033	0.083
Sampling point 10	0.018	0.048	0.010	0.018	0.059
Sampling point 11	0.040	0.071	0.014	0.040	0.059
Sampling point 12	-0.011	0.019	0.005	-0.011	0.062

The test results show that in the system error of the test device, $\overline{\mu_B}$, was basically zero, m_B did not exceed 0.12 mm, σ_B did not exceed 0.014 mm, R_B did not exceed 0.057 mm, and D_B did not exceed 0.13 mm. Thus, the test device had high accuracy and precision.

Fig. 17 shows the distribution of the error data. The horizontal axis represents the sampling sequence, and the vertical axis represents the measurement error in millimeters.

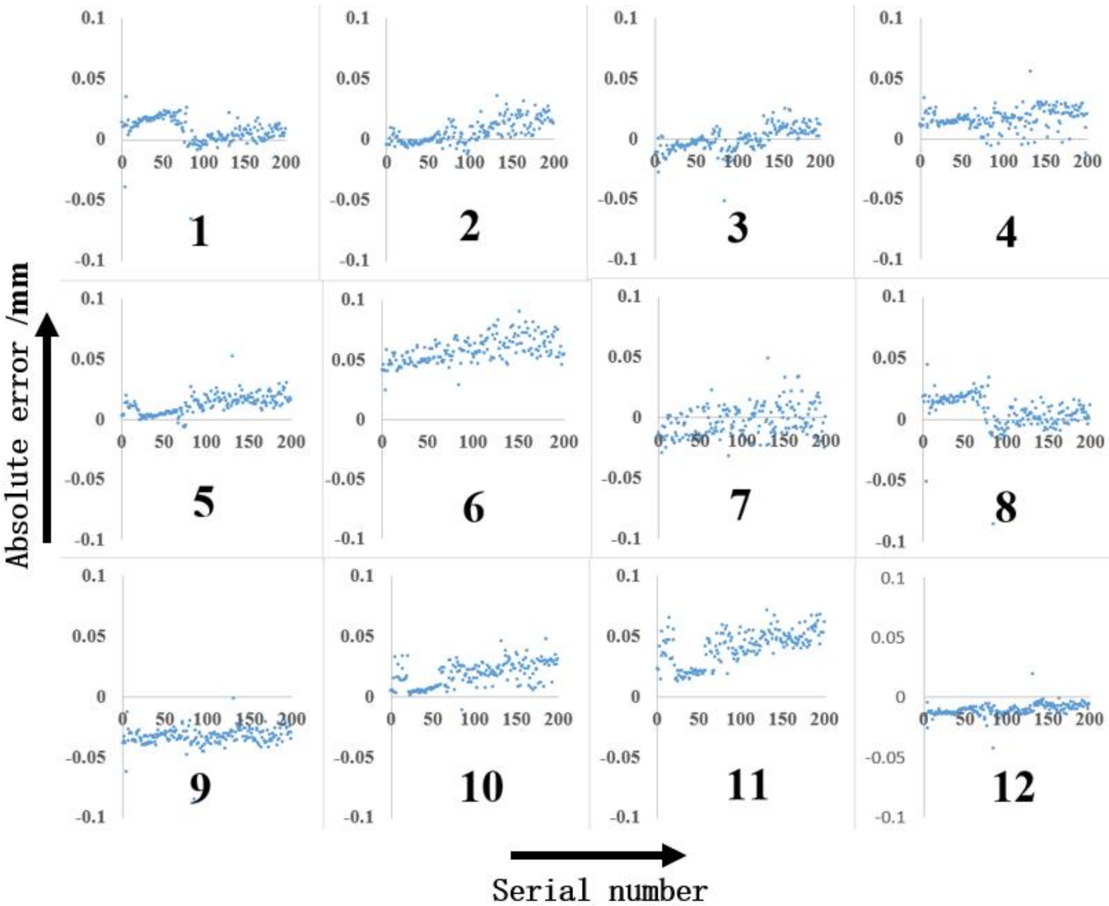

Fig. 17 Error distribution of repeated measurement sampling

3.6 Field width measurement test

The frame of the visual measurement test platform was constructed using aluminum profiles. The main equipment included two MV-EM510C industrial cameras (resolution 2,456 × 2,058), the focal length of the lens was 8 mm, and the distance between the camera lens and the dam surface was approximately 240 mm. When installed, the visual axis was perpendicular to the surface of the dam. A digital vernier caliper with an accuracy of 0.01 mm was used to measure the crack width on site for comparison data. The proposed algorithm for determining the measurement direction was used to obtain the measurable points in the crack. Then, five of the measurable points were randomly selected for width measurement, and the measurement position was marked in the real-time image of the left camera. Subsequently, the digital display vernier caliper was used to measure the inner diameter of the crack to obtain the standard value of its width at that location, as shown in Fig 18. The visual measurement value was used for comparison with the standard value. Referring to the experiments in previous studies [26,43,45], the absolute error was used to measure the accuracy of the proposed measurement method.

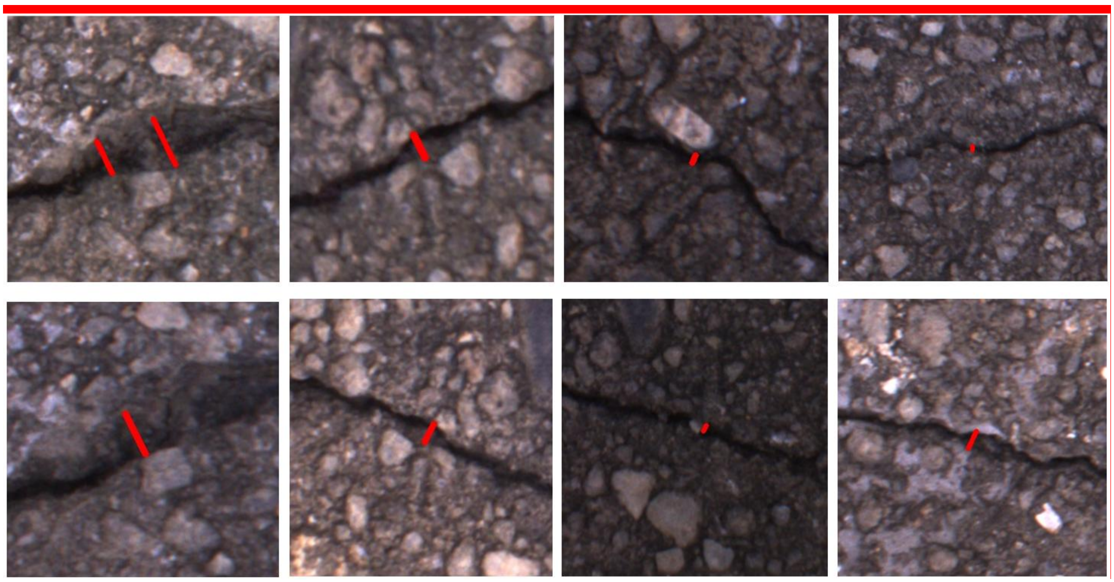

Fig. 18 Field measurement test

A total of nine groups were measured in this experiment. The deviation between the width value measured by the visual measurement and the standard value measured by the digital vernier caliper is shown in Fig. 19. The average absolute error, $\bar{\mu}$, and the standard deviation, σ, of the absolute error of each group of data are shown in Table 6.

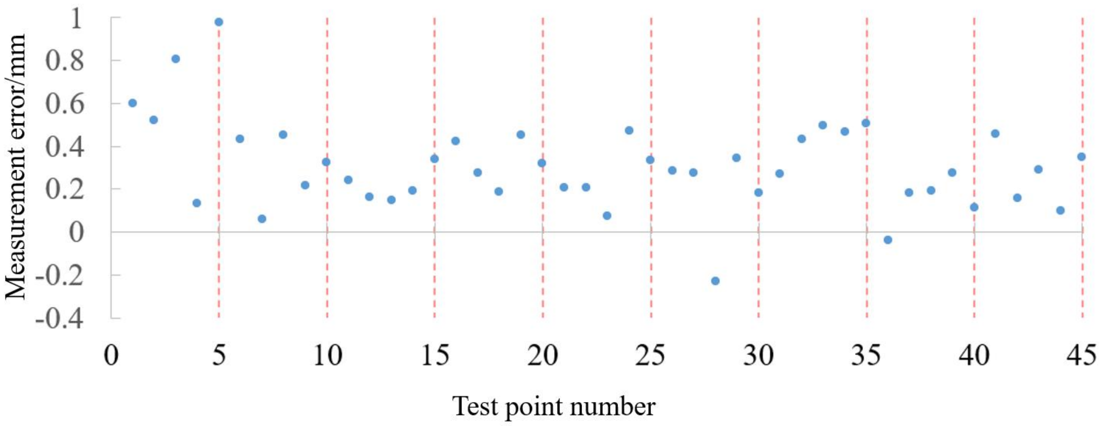

Fig. 19 Deviation of the width value of the visual measurement from the standard value

Table 6. Width measurement error average and standard deviation

Group	Error/(mm)	$\bar{\mu}$ /(mm)	σ /(mm)	Group	Error/(mm)	$\bar{\mu}$ /(mm)	σ /(mm)
	0.60				0.28		
	0.52				0.28		
1	0.81	0.61	0.32	6	-0.23	0.26	0.06
	0.13				0.35		
	0.98				0.18		
	0.43				0.27		
	0.06				0.43		
2	0.45	0.30	0.16	7	0.50	0.43	0.10
	0.22				0.47		
	0.33				0.51		
3	0.24	0.22	0.09	8	-0.04	0.16	0.09

	0.16				0.18		
	0.15				0.19		
	0.19				0.28		
	0.34				0.11		
	0.42				0.46		
	0.28				0.16		
4	0.19	0.33	0.11	9	0.29	0.27	0.14
	0.45				0.10		
	0.32				0.35		
	0.21						
	0.21			$\overline{\mu}$ mean = 0.32 mm			
5	0.07	0.26	0.15				
	0.47			σ mean = 0.19 mm			
	0.34						

In Fig. 19 and Table 6, the results show that the average error of this test was approximately 0.32 mm, and the average variance was 0.19 mm. This demonstrates that the visual measurement test results in this study are close to those of commonly used methods in engineering, which indicates that the proposed method can be utilized in engineering applications.

4 Conclusion

This study proposed a practical and complete visual method for measuring crack width using a real dam as the research object. The effectiveness of U-Net in the task of crack segmentation was first verified. Then, to address the problem of data redundancy in the crack skeleton, this study designed a more streamlined and stable crack backbone extraction method. The total number of eight-neighborhood points of each point on the backbone did not exceed two, which reduced the amount of backbone data and the distribution types of the eight neighborhoods of backbone points. The backbone's ability to describe the shape of cracks was also enhanced. Furthermore, we designed a more accurate method for determining the direction of the crack width measurement by combining the slope characteristics at the backbone macroscale feature and the neighborhood distribution characteristics at the microscale feature. We further defined the crack width visual measurement method according to the measurement direction.

To evaluate the advantages and disadvantages of the measurement methods, two criteria (i.e., recall rate of measurement direction and direction error) were added to provide a technical reference for subsequent research. Then, we conducted a series of experiments to verify that the proposed crack backbone extraction algorithm has a good streamlining effect compared to the Zhang–Suen image-refinement algorithm. Compared with the method presented by Luo et al. [46], we demonstrated that our proposed method obtains a more accurate width measurement direction. From the width measurement test, we also demonstrated that it has prospects for practical engineering applications, and the intelligent degree of structural health monitoring and repair was improved. The proposed method also provides a reference for the radial vision measurements of other slender and irregular targets.

In the future, for structural damage (e.g., cracks), research on faster, lighter, more accurate, and more stable image segmentation methods based on U-Net is needed. The visual measurement process should also be streamlined on the basis of the existing framework to improve the efficiency of the algorithm. Finally, the three-dimensional reconstruction of cracks should be explored to improve measurement accuracy and depth measurements so that vision systems will inherit more comprehensive crack-damage detection capabilities.

Acknowledgments

This research was funded by the National Natural Science Foundation of China (Grant No. U2006224, 52108199), China Postdoctoral Science Foundation (2021M690765), Science and Technology Planning Project of Guangzhou (202102080269), Natural Science Foundation of Guangxi Province (2021GXNSFAA220045), and Systematic Project of Guangxi Key Laboratory of Disaster Prevention and Engineering Safety (2021ZDK007).

Appendix A. Examples of processing procedures

Process	Result	Process	Result
Original		Binarized by U-Net	
Backbone refinement	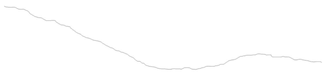	Curve fitting in Macro scale	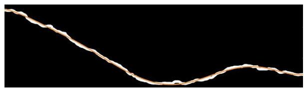
Distance to measuring surface	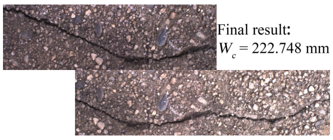	Width measurement	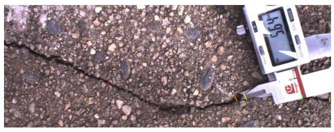
P1(783, 1023)	Measurement point 1: (788,1013); Measurement point 2: (778,1033);	Measurement direction: 67.5° Width = 1.936 mm	
P2(1742, 1143)	Measurement point 1: (1731,1121); Measurement point 2: (1749,1158);	Measurement direction: 112.5° Width = 3.563 mm	
P3(1808, 1119)	Measurement point 1: (1796,1095); Measurement point 2: (1822,1148);	Measurement direction: 112.5° Width = 5.112 mm	
P4(2242, 1126)	Measurement point 1: (2242,1117); Measurement point 2: (2242,1140);	Measurement direction: 90° Width = 1.992 mm	
P5(2446, 1147)	Measurement point 1: (2446,1138); Measurement point 2: (2446,1156);	Measurement direction: 90° Width = 1.559 mm	

References

[1] G. Grzegorz, Evaluation of fracture processes under shear with the use of DIC technique in fly ash concrete and accurate measurement of crack path lengths with the use of a new crack tip tracking method, Measurement. (2021) 109632.

[2] H. Kim, E. Ahn, M. Shin, S.-H. Sim, Crack and noncrack classification from concrete surface images using machine learning, Structural Health Monitoring. 18 (2019) 725–738.

[3] C.-Z. Dong, F.N. Catbas, A review of computer vision–based structural health monitoring at local and global levels, Structural Health Monitoring. (2020) 1475921720935585.

[4] Q. Gong, L. Zhu, Y. Wang, Z. Yu, Automatic subway tunnel crack detection system based on line scan camera, Structural Control and Health Monitoring. (2021).

[5] B. Li, J. Yang, D. Hu, Dam monitoring data analysis methods: A literature review, Structural Control and Health Monitoring. 27 (2020) e2501.

[6] Z. Chen, X. Huang, S. Yu, W. Cao, W. Dang, Y. Wang, Risk analysis for clustered check dams due to heavy rainfall, International Journal of Sediment Research. 36 (2021) 291–305.

[7] E. Zhao, C. Wu, Risk probabilistic assessment of ultrahigh arch dams through regression panel modeling on deformation behavior, Structural Control and Health Monitoring. 28 (2021) e2716.

[8] D. Proske, Comparison of dam failure frequencies and failure probabilities, Beton-und

Stahlbetonbau. 113 (2018) 2–6.
[9] X. Li, Z. Li, R. Feng, S. Luo, C. Zhang, M. Jiang, H. Shen, Generating high-quality and high-resolution seamless satellite imagery for large-scale urban regions, Remote Sensing. 12 (2020) 81.
[10] Y. Tang, A. Zhang, L. Luo , G. Wang, E. Yang, Pixel-level pavement crack segmentation with encoder-decoder network. Measurement. 184 (2021) 109914.
[11] Z. Liu, B. Gao, G.Y. Tian, Natural crack diagnosis system based on novel L-shaped electromagnetic sensing thermography, IEEE Transactions on Industrial Electronics. 67 (2019) 9703–9714.
[12] J. Pang, H. Zhang, C. Feng, L. Li, Research on crack segmentation method of hydro-junction project based on target detection network, KSCE Journal of Civil Engineering. 24 (2020) 2731–2741.
[13] A. Kocherla, M. Duddi, K.V.L. Subramaniam, Embedded PZT sensors for monitoring formation and crack opening in concrete structures, Measurement. (2021) 109698.
[14] Y. Xu, Z. Zhou, B. Zhang, Application of bionic crack monitoring in concrete bridges, Journal of Highway and Transportation Research and Development (English Edition). 6 (2012) 44–49.
[15] H.N. Nguyen, T.Y. Nguyen, D.L. Pham, Automatic measurement of concrete crack width in 2D multiple-phase images for building safety evaluation, in: Asian Conference on Intelligent Information and Database Systems, Springer, 2018: pp. 638–648.
[16] S. Yu, J. Zhang, X. He, An advanced vision-based deformation measurement method and application on a long-span cable-stayed bridge, Measurement Science and Technology. 31 (2020) 065201.
[17] J.S. Lee, S.H. Hwang, I.Y. Choi, Y. Choi, Estimation of crack width based on shape-sensitive kernels and semantic segmentation, Structural Control and Health Monitoring. 27 (2020).
[18] B. Ferrer, J. Espinosa, D. Mas, A method to measure small local strains in concrete surfaces using its natural texture and image cross-correlation, Structural Control and Health Monitoring. 26 (2019) e2410.
[19] X. Shao, Z. Chen, X. Dai, X. He, Camera array-based digital image correlation for high-resolution strain measurement, Review of Scientific Instruments. 89 (2018) 105110.
[20] Y. Chi, L. Yu, B. Pan, Low-cost, portable, robust and high-resolution single-camera stereo-DIC system and its application in high-temperature deformation measurements, Optics and Lasers in Engineering. 104 (2018) 141–148.
[21] B. Pan, Digital image correlation for surface deformation measurement: historical developments, recent advances and future goals, Measurement Science and Technology. 29 (2018) 82001.
[22] X. Li, H. Shen, H. Li, L. Zhang, Patch matching-based multitemporal group sparse representation for the missing information reconstruction of remote-sensing images, IEEE Journal of Selected Topics in Applied Earth Observations and Remote Sensing. 9 (2016) 3629–3641.
[23] H. Perez, J. Tah, Deep learning smartphone application for real-time detection of defects in buildings, Structural Control and Health Monitoring. 28 (2021) e2751 .
[24] M. Chen, Y. Tang, X. Zou, K. Huang, L. Li, Y. He, High-accuracy multi-camera reconstruction enhanced by adaptive point cloud correction algorithm, Optics and Lasers in Engineering. 122

(2019) 170–183.

[25] Y.-C. Tang, L.-J. Li, W.-X. Feng, F. Liu, X.-J. Zou, M.-Y. Chen, Binocular vision measurement and its application in full-field convex deformation of concrete-filled steel tubular columns, Measurement. 130 (2018) 372–383.

[26] W. Wang, A. Zhang, K.C.P. Wang, A.F. Braham, S. Qiu, Pavement crack width measurement based on Laplace's equation for continuity and unambiguity, Computer-Aided Civil and Infrastructure Engineering. 33 (2018) 110–123.

[27] Q. Zou, Z. Zhang, Q. Li, X. Qi, Q. Wang, S. Wang, Deepcrack: Learning hierarchical convolutional features for crack detection, IEEE Transactions on Image Processing. 28 (2018) 1498–1512.

[28] A. Zhang, K.C.P. Wang, Y. Fei, Y. Liu, C. Chen, G. Yang, J.Q. Li, E. Yang, S. Qiu, Automated pixel-level pavement crack detection on 3D asphalt surfaces with a recurrent neural network, Computer-Aided Civil and Infrastructure Engineering. 34 (2019) 213–229.

[29] M. Wang, J.C.P. Cheng, A unified convolutional neural network integrated with conditional random field for pipe defect segmentation, Computer-Aided Civil and Infrastructure Engineering. 35 (2020) 162–177.

[30] A. Rezaie, R. Achanta, M. Godio, K. Beyer, Comparison of crack segmentation using digital image correlation measurements and deep learning, Construction and Building Materials. 261 (2020) 120474.

[31] N.-D. Hoang, Detection of surface crack in building structures using image processing technique with an improved Otsu method for image thresholding, Advances in Civil Engineering. 2018 (2018).

[32] Y. Noh, D. Koo, Y.-M. Kang, D. Park, D. Lee, Automatic crack detection on concrete images using segmentation via fuzzy C-means clustering, in: 2017 International Conference on Applied System Innovation (ICASI), IEEE, 2017: pp. 877–880.

[33] H. Kim, E. Ahn, S. Cho, M. Shin, S.-H. Sim, Comparative analysis of image binarization methods for crack identification in concrete structures, Cement and Concrete Research. 99 (2017) 53–61.

[34] A. Garcia-Garcia, S. Orts-Escolano, S. Oprea, V. Villena-Martinez, J. Garcia-Rodriguez, A review on deep learning techniques applied to semantic segmentation, ArXiv Preprint ArXiv:1704.06857. (2017).

[35] C.V. Dung, Autonomous concrete crack detection using deep fully convolutional neural network, Automation in Construction. 99 (2019) 52–58.

[36] Y.-J. Cha, W. Choi, Vision-based concrete crack detection using a convolutional neural network, in: Dynamics of Civil Structures, Volume 2, Springer, 2017: pp. 71–73.

[37] Y. Cha, W. Choi, O. Büyüköztürk, Deep learning-based crack damage detection using convolutional neural networks, Computer-Aided Civil and Infrastructure Engineering. 32 (2017) 361–378.

[38] H. Ju, W. Li, S. Tighe, Z. Xu, J. Zhai, CrackU-net: A novel deep convolutional neural network for pixelwise pavement crack detection, Structural Control and Health Monitoring. (2020) e2551.

[39] A. Zhang, K.C.P. Wang, B. Li, E. Yang, X. Dai, Y. Peng, Y. Fei, Y. Liu, J.Q. Li, C. Chen, Automated pixel-level pavement crack detection on 3D asphalt surfaces using a deep-learning network,

Computer-Aided Civil and Infrastructure Engineering. 32 (2017) 805–819.
[40] A.A. Diana, N. Anand, A.G. Prince, A novel approach for thermal crack detection and quantification in structural concrete using ripplet transform, Structural Control and Health Monitoring. 27 (2020).
[41] M. Payab, R. Abbasina, M. Khanzadi, A brief review and a new graph-based image analysis for concrete crack quantification, Archives of Computational Methods in Engineering. 26 (2019) 347–365.
[42] Y. Yan, Z. Mao, J. Wu, T. Padir, J.F. Hajjar, Towards automated detection and quantification of concrete cracks using integrated images and lidar data from unmanned aerial vehicles, Structural Control and Health Monitoring. (2021) e2757.
[43] S. Qiu, W. Wang, S. Wang, K.C.P. Wang, Methodology for accurate AASHTO PP67-10–based cracking quantification using 1-mm 3D pavement images, Journal of Computing in Civil Engineering. 31 (2017) 04016056.
[44] A.H. Asjodi, M.J. Daeizadeh, M. Hamidia, K.M. Dolatshahi, Arc Length method for extracting crack pattern characteristics, Structural Control and Health Monitoring. (2020).
[45] H. Kim, J. Lee, E. Ahn, S. Cho, M. Shin, S.-H. Sim, Concrete crack identification using a UAV incorporating hybrid image processing, Sensors. 17 (2017) 2052.
[46] Q. Luo, B. Ge, Q. Tian, A fast adaptive crack detection algorithm based on a double-edge extraction operator of FSM, Construction and Building Materials. 204 (2019) 244–254.
[47] B. Dai, C. Gu, E. Zhao, K. Zhu, W. Cao, X. Qin, Improved online sequential extreme learning machine for identifying crack behavior in concrete dam, Advances in Structural Engineering. 22 (2019) 402–412.
[48] C. Feng, H. Zhang, H. Wang, S. Wang, Y. Li, Automatic pixel-level crack detection on dam surface using deep convolutional network, Sensors. 20 (2020) 2069.
[49] O. Ronneberger, P. Fischer, T. Brox, U-net: Convolutional networks for biomedical image segmentation, in: International Conference on Medical Image Computing and Computer-Assisted Intervention, Springer, 2015: pp. 234–241.
[50] S.L.H. Lau, E.K.P. Chong, X. Yang, X. Wang, Automated pavement crack segmentation using u-net-based convolutional neural network, IEEE Access. 8 (2020) 114892–114899.
[51] Z. Liu, Y. Cao, Y. Wang, W. Wang, Computer vision-based concrete crack detection using U-net fully convolutional networks, Automation in Construction. 104 (2019) 129–139.
[52] Z. Zhang, Q. Liu, Y. Wang, Road extraction by deep residual u-net, IEEE Geoscience and Remote Sensing Letters. 15 (2018) 749–753.
[53] T.Y. Zhang, C.Y. Suen, A fast parallel algorithm for thinning digital patterns, Communications of the ACM. 27 (1984) 236–239.

Novel visual crack width measurement based on backbone double-scale features for improved detection automation

Yunchao Tang[1,2,3*], Zhaofeng Huang[4], Zheng Chen[1,2*], Mingyou Chen[4], Hao Zhou[4], Zhang Hexin[5], Sun Junbo[6]

[1] *Guangxi Key Laboratory of Disaster Prevention and Engineering Safety, School of Civil Engineering and Architecture, Guangxi University, Nanning 530004, China*;

[2] *Key Laboratory of Disaster Prevention and Structural Safety of Ministry of Education, School of Civil Engineering and Architecture, Guangxi University, Nanning 530004, China*;

[3] *College of Urban and Rural Construction, Zhongkai University of Agriculture and Engineering, Guangzhou, Guangdong* 510006, *China;*

[4] *College of Engineering, South China Agricultural University, Guangzhou, Guangdong* 510642, *China;*

[5] *School of Engineering and the Built Environment, Edinburgh Napier University, 10 Colinton Road, Edinburgh, Scotland, UK, EH10 5DT*

[6] *School of Design and Built Environment, Curtin University, Perth, WA 6102, Australia;*

Abstract: State-of-the-art machine-vision systems have limitations associated with crack width measurements. The sample points used to describe the crack width are often subjectively defined by experimenters, which obscures the crack width ground truth. Consequently, in most related studies, the uncontrollable system errors of vision modules result in unsatisfactory measurement accuracy. In this study, the cracks of a reservoir dam are taken as objects, and a new crack backbone refinement algorithm and width-measurement scheme are proposed. The algorithm simplifies the redundant data in the crack image and improves the efficiency of crack-shape estimation. Further, an effective definition of crack width is proposed that combines the macroscale and microscale characteristics of the backbone to obtain accurate and objective sample points for width description. Compared with classic methods, the average simplification rate of the crack backbone and the average error rate of direction determination are all improved. The results of a series of experiments validate the efficacy of the proposed method by showing that it can improve detection automation and has potential engineering application.

Key words: Concrete crack; Image thinning; Machine vision; Multi-scale feature fusion

1 Introduction

Cracks are a common type of structural damage that jeopardize the health of concrete buildings (e.g., roads, bridges, tunnels, and dams) [1–5]. Regular inspections and repairs can reduce the risk of structural collapse during natural disasters (e.g., earthquakes and floods) [6–10].

Researchers have proposed a variety of innovative methods to replace traditional manual visual inspection [11–14]. However, their methods target larger, more complex field-environment crack detection tasks that are expensive, slow and susceptible to external interference [15–18]. Non-contact, high-precision computer-assisted visual measurement has shown good performance in various inspection fields [19–23] and is a promising method to replace human visual inspections. Researchers have provided a relatively complete process framework for mapping image pixel features to geometric dimensions in real physical space [24,25]. However, for complex slender and irregular targets, such as cracks, the current measurement applications lack geometric meaning, and their accuracy is not sufficient [26].

Regarding the identification and segmentation of cracks, researchers have applied the classic digital image processing (DIP) method and neural-network models to make the extraction of cracks more robust [27–32]. Kim et al. [33] compared the threshold segmentation effects of five classic threshold segmentation algorithms on concrete cracks and showed that the less robust threshold segmentation suffers background complexity, large changes in illumination, and inconsistencies. It is generally difficult to accurately detect cracks under uniform conditions. Other researchers have proposed semantic segmentation models that have been effective in solving these problems [34–37]. Many scholars have also proposed corresponding model structures specifically for crack detection. For example, Zou et al. developed the DeepCrack [27] network based on SegNet and achieved an F-measure greater than 0.87. They improved the segmentation accuracy but introduced larger scale parameters. Ju et al. developed the CrackU-net [38] model, which improved on U-Net and FCN and achieved an accuracy of 99.01%. Wang and Cheng combined DilaSeg and RNN and proposed DilaSeg-CRF [29] for segmentation cracks, which achieved a 20% to 32% improvement compared to the classic semantic segmentation model. Zhang et al. designed CrackNet [39] without a pooling layer in an attempt to reduce the accuracy loss in the crack segmentation process. Then, they combined it with an RNN and proposed CrackNet-R [28] to improve the accuracy of segmentation, subsequently obtaining a higher recall rate and F-measure. These neural-network methods were optimized for concrete cracks and provided more opportunities for improvement. However, increasing the network depth to improve accuracy increases the burden on the hardware in the application process.

The quantitative analysis of crack-hazard degree (e.g., crack length, width, and depth) is presently insufficient [17,40]. For example, clearly defining a crack width from a visual measurement and continuously performing such measurements remain quite challenging [26,41,42]. Historically, researchers used an edge or a skeleton of the crack as the basis for width measurement [43], but several problems remain. For example, the two edges of a crack may be quite different in the local area, and it is difficult to obtain accurate measurement directions. The crack skeletons obtained by improved refinement algorithms must still handle redundant data, and the definition of the skeleton remains inaccurate.

Researchers have attempted to use these features to define the crack-width visual measurement method and achieved varying results. For example, Asjod et al. [44] proposed the arc-length method to measure cracks. Further, Wang et al. [26] proposed a Laplace-based continuous explicit measurement method that simulates the crack as an electric field in a capacitor, and used the total length of the trajectory of electrons in the cathode and anode of a capacitor to define the width of the crack. However, the width obtained by their method is the length of a curve, not a straight-line distance needed for engineering. Kim et al. [45] proposed using the two edge points closest to the crack skeleton point for width measurement. Luo et al. [46] investigated the crack edges from the crack skeleton point in four directions and took the minimum distance between the two edges in the four directions as the width of the crack. Their method performs well with idealized cracks. However, in reality, the width often refers to the straight-line distance between the two edges in the normal direction of the crack-growth direction, and the crack edges often have irregular bumps. Hence, the two edges are not strictly symmetrical about the skeleton.

The above methods use measurement points that do not match the geometric meaning of width. Therefore, the measurement correctness must be improved. The comprehensiveness of using only numerical results as the evaluation criteria of measurement methods needs to be improved. In addition, whereas many studies have focused on road cracks, only a few have focused on dam cracks, which have characteristics of large image noise, complex background texture, and random location [47,48]. The research object needs to be expanded, thus, a large scope exists for machine-vision measurement research in this area.

In this study, we selected a reservoir dam crack located in the field as the research object and developed a more streamlined crack backbone extraction algorithm, based on an improved image-refinement algorithm, that enhances the backbone's ability to describe crack shapes. Further, we devised a more accurate measurement direction by combining the backbone macroscale slope characteristics and microscale neighborhood distribution characteristics. Then, defining the width of the crack as the straight-line distance between two measurement points located at the edge of the crack in the measurement direction, we developed a crack-width measurement method. Two evaluation criteria are included: the measurement recall rate and direction error. Compared with the method proposed by Luo et al. [46], the method proposed here is more comprehensive, in that it has a more accurate visual measurement performance that aligns with the geometric meaning of width. This study makes the following contributions:

1. A detailed visual crack width measurement process is proposed that can provide stable and continuous measurements.

2. Based on the improved image-refinement algorithm used to further refine the complete crack backbone, the neighborhood distribution types of backbone points are reduced to facilitate their use in classifying backbone points.

3. Combining the macro and micro characteristics of the backbone, a visual crack width measurement method that is closer to the actual needs of the project is used to obtain a more accurate measurement method.

4. Two evaluation measurement standards (i.e., recall rate and direction error) are added to enable a more comprehensive evaluation of the measurement method.

The remainder of this article is structured as follows. The process and principle of the crack width measurement method are described in Section 2. Section 3 presents the relevant evaluation test conducted on the proposed method. Section 4 provides concluding remarks and outlines possible future study.

2 Methods

2.1 Visual crack-measurement process

The basic processes of the width-measurement method proposed in this study include crack segmentation, backbone refining, and width measurement. The specific process is shown in Fig. 1. Previous studies have shown that the U-Net semantic segmentation model is sensitive to edge detail features, which also suggests that it would be suitable for dam-crack segmentation [49–52]. In this article, the input into U-Net was an RGB image and the output is a semantically segmented binary image. The process of semantic segmentation takes place in a code-decoded symmetrical U-shaped structural model, hence the name U-Net. The acquisition of the parameters in the U-shaped structural model requires convolutional inference of a large number of labeled samples, the result of which is then recorded in the model file. When using U-Net, this model file is called and the image data is passed into the model. The segmentation result can be obtained after calculation by U-Net, which is a very simple and commonly used semantic segmentation model. In this study, the results of the U-Net semantic segmentation model were therefore directly used as the input material for the pretreatment of the crack backbone extraction and crack width measurement. Pretreatment can effectively handle possible misjudgment problems in crack segmentation while improving the robustness of backbone refining. Morphology (large) represents the morphological processing of the large window, which is used for the segmentation of the crack area; morphology (small) represents small window morphology processing, which is used to strengthen the connectivity of the crack binary image. Morphological processing here referes to dilation or erosion algorithms (they have opposite effects to each other), whose role is to expand the binarized target towards the background. Combinatorial binarization is the combined operation of binarization–blur–binarization, which is used to smooth the crack binary image and eliminate segmentation impurities before backbone extraction. The role of blur is also to expand the target, but its effect is more moderate than that of morphological processing.

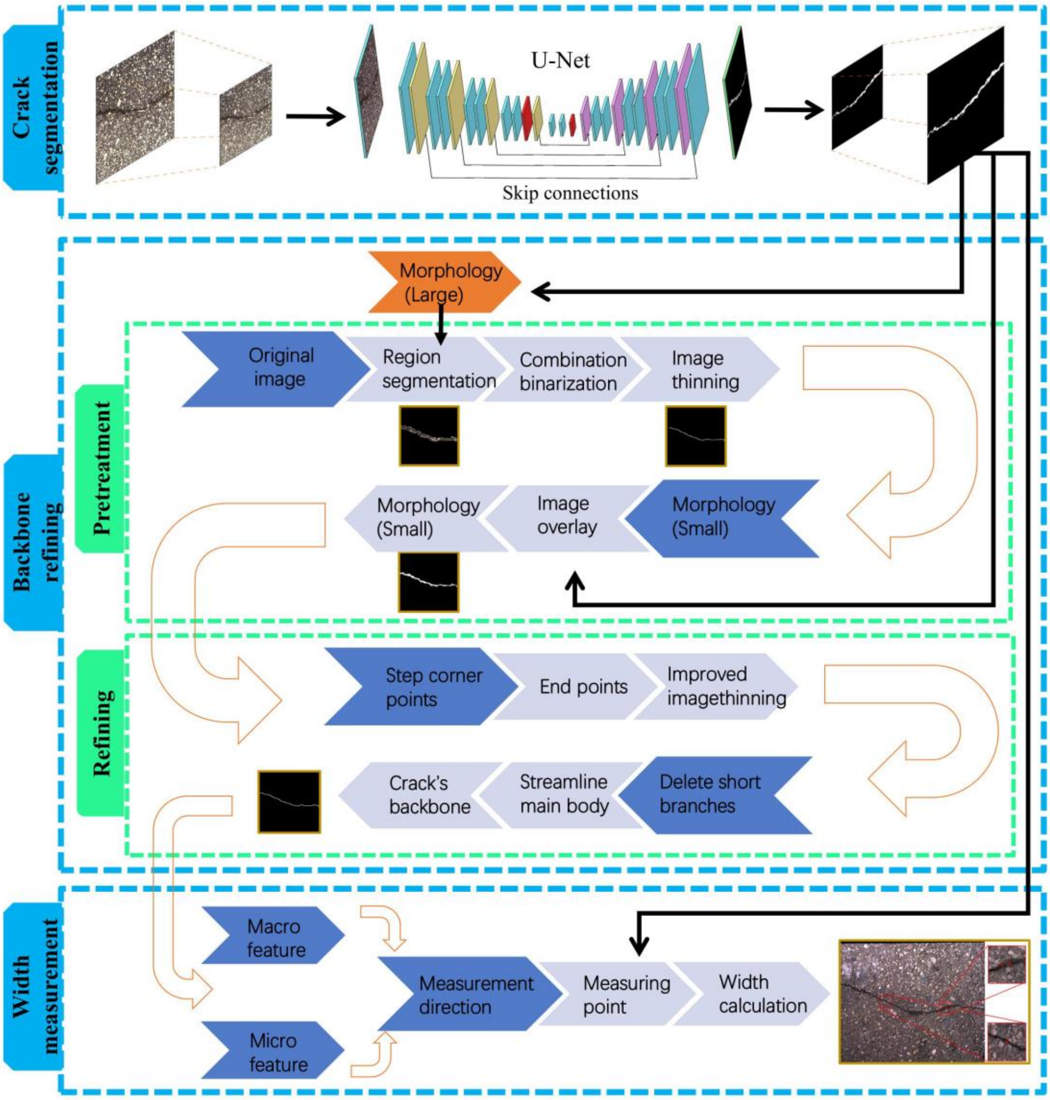

Fig. 1 Framework and flowchart for visual measurement

2.2 Crack backbone refinement

To address the problem of redundant data points when the image-refinement algorithm extracts the crack skeleton, we refine the crack skeleton and the backbone of the crack using the improved image-refinement algorithm to mark the ends of the cracks while avoiding end-shortening during refinement. The refinement of the crack backbone removes redundant points on the branches and backbones based on the skeleton.

The backbone of the crack contains information on the shape of the crack, which has the function of determining its position and providing the basis for measuring its width. The classic Zhang–Suen image thinning algorithm [53] can be used to extract the crack skeleton, but the skeleton still has redundant data, which can be further streamlined to obtain the backbone of the crack. For the convenience of comparison and explanation in this work, it is stipulated that the output of the Zhang-Suen image thinning algorithm is called "skeleton", and the output proposed for improvement and further processing based on the Zhang-Suen image thinning algorithm is called "backbone".

The input into the crack backbone refinement algorithm is a crack binary image with only crack and background pixels. This process involves iterative refinement. In each iteration, the outermost contour is transformed into the background. The algorithm sets a certain crack pixel as $P0$. Starting from the pixel just above $P0$, the eight neighborhoods of $P0$ are set as $P1$ to $P8$, clockwise. The background point is assigned a value of either zero or one, as shown in Fig. 2.

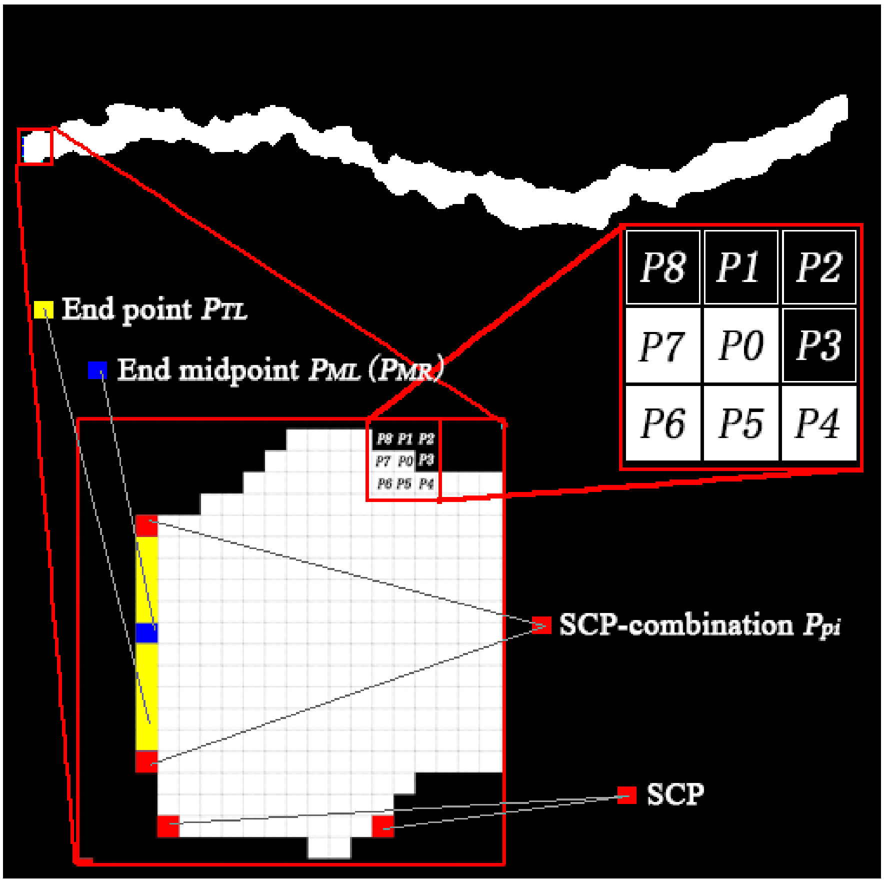

Fig. 2 Feature points in crack binary graph

Detecting the edge of the crack binary image involves multiple steps. As shown in Fig. 2, each step with a vertex height greater than 1 pixel is the step corner point (SCP), which can be found according to its eight-neighborhood features and is used to build set CoP. Let $P_0(\Delta P)$ denote the set of P_0's eight neighborhoods satisfying condition ΔP. The set, CoP, is given by the formula $CoP = \left\{ P_0 \middle| P_0\left(\Delta P\right) \right\}$, in which ΔP is defined by Eq. (1):

$$\begin{aligned} &\exists\left(P_1 + P_2 + P_3 = 3 \wedge P_5 + P_6 + P_7 + P_8 = 0\right) \\ &\vee\left(P_3 + P_4 + P_5 = 3 \wedge P_1 + P_6 + P_7 + P_8 = 0\right) \\ &\vee\left(P_5 + P_6 + P_7 = 3 \wedge P_1 + P_2 + P_3 + P_4 = 0\right) \\ &\vee\left(P_7 + P_8 + P_1 = 3 \wedge P_2 + P_3 + P_4 + P_5 = 0\right), \quad P_0 \in P_0\left(\Delta P\right) \end{aligned}, \qquad (1)$$

In CoP, the two SCPs in the same column are recorded as a set, P_{pi}, and its midpoint, P_{piM}, is marked from there, as shown in Fig. 2. Then, according to the eight-neighborhood feature, the P_{piM} in the left and right ends of the crack, which are regarded as P_{ML} and P_{MR}, can be separated from the set of all P_{piM}. P_{ML} and P_{MR}'s eight neighborhoods at the left and right ends to satisfy Eq. (2).

$$\begin{aligned} &(a) P_6 + P_7 + P_8 = 0 \Rightarrow P_{ML} \\ &(b) P_2 + P_3 + P_4 = 0 \Rightarrow P_{MR} \end{aligned}, \qquad (2)$$

The pixels in the same column as P_{ML} or P_{MR} are the crack's end points—recorded as P_{TL} and P_{TR}, respectively. If P_{TL} and P_{TR}'s eight neighborhoods satisfy the condition $P_1 + P_5 = 2$, they are respectively recorded in sets $TePL$ and $TePR$. The purpose of this move is to eliminate the points overlapping the edges among the endpoints during the refinement process.

Let $A(P_0)$ denote the number of 01 patterns of the clockwise connections in the eight neighborhoods of P_0 and $B(P_0)$ denote the number of crack pixels in the eight neighborhoods of P_0. One iteration of the crack backbone extraction algorithm is divided into odd- and even-numbered sub-iterations. In each sub-iteration, the crack pixels that satisfy Eq. (3) are marked as the outermost pixels, which are uniformly converted into background pixels before the iteration completes. In even-numbered sub-iterations, only conditions (c), (d), and (e) are respectively changed to (c’), (d’), and (e’).

$$\begin{array}{l} (a)\, A(P_0)=1 \\ (b)\, 2 \le B(P_0) \le 6 \\ (c)\, P_1 \times P_3 \times P_5 = 0 \\ (d)\, P_3 \times P_5 \times P_7 = 0 \\ (e)\, P_0 \notin TePR \\ (c')\, P_1 \times P_3 \times P_7 = 0 \\ (d')\, P_1 \times P_5 \times P_7 = 0 \\ (e')\, P_0 \notin TePL \end{array}, \tag{3}$$

The algorithm iteratively thins the cracks to obtain the skeleton according to the above rules until no crack pixels are marked as outermost pixels. However, there are still numerous redundant points in the skeleton that can be streamlined further. The streamlining process is divided into two steps: deleting short branches and streamlining the skeleton’s main body to obtain the backbone.

To delete short branches, the skeleton’s endpoints are marked on the left and right sides of the image and other endpoints satisfying $B(P_0) < 2$, or $B(P_0) = 2$ and $A(P_0) = 1$, apart from the skeleton’s endpoints. Once an end point is deleted on the short branch, the connected point becomes the new endpoint. These operations are repeated several times until all short branches are deleted. The deletion process is illustrated in Fig. 3.

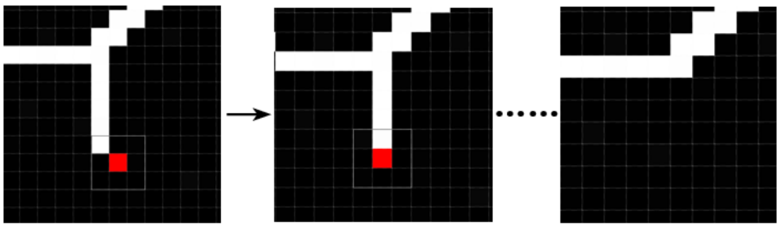

Fig. 3 Short branch deletion process

The refinement of the backbone is to convert pixels in the skeleton line that satisfy any of the items in Eq.(4) to the background. If the image is scanned from the first pixel in the upper left corner to the last pixel in the lower right corner, then, as shown in Fig. 4, the red pixels are deleted. After cleaning, the backbone is obtained with the following features:

(1) The total number of backbone pixels in each point's eight-neighborhood does not exceed 2.

(2) Its eight-neighborhood pixel distribution will show four shapes: v shape, linear shape, semi-Y shape of left and semi-Y shape of right. Plus, when each shape is rotated around the center, the number of neighborhood distribution types of backbone points is reduced to $C_4^2 + C_2^1 + C_4^1 C_2^1 = 16$, as shown in the lower right corner of Fig. 4.

$$\begin{aligned} &(a) P_1 + P_3 = 2 \\ &(b) P_1 + P_7 = 2 \\ &(c) P_5 + P_3 = 2 \\ &(d) P_5 + P_7 = 2 \end{aligned}, \tag{4}$$

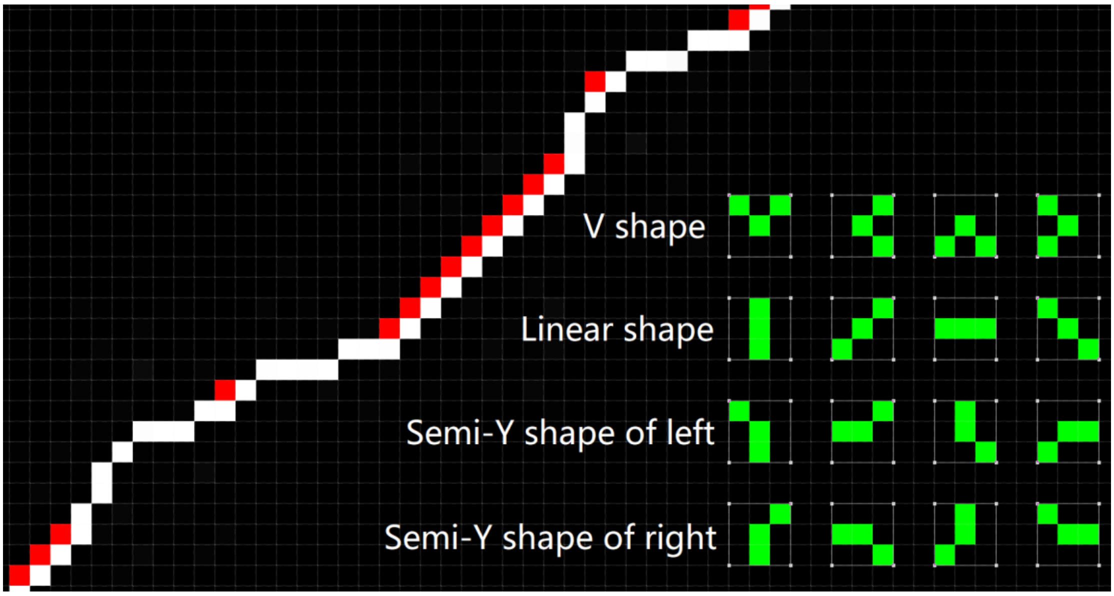

Fig. 4 Streamlined backbone

Fig. 5 illustrates the effect of the main crack extraction. The backbone extraction algorithm in this paper is more streamlined than others. In total, compared with the classic Zhang-Suen image thinning algorithm, the crack backbone refinement algorithm in this paper has the following characteristics:

1. The branches are removed and the shape of the end of the crack is retained (as shown in the upper left corner of Fig. 5a and upper right corner of Fig. 5b);

2. The eight-neighborhood effective pixels of the backbone do not exceed 2 and there are

only 16 types of neighborhood pixel distribution (as shown in the lower right corner of Fig. 4 and the lower right corner of Fig. 5).

While simplifying the amount of data, it is convenient to use the neighborhood distribution type to classify the backbone points, which is conducive to the subsequent clear definition of the crack-width measurement.

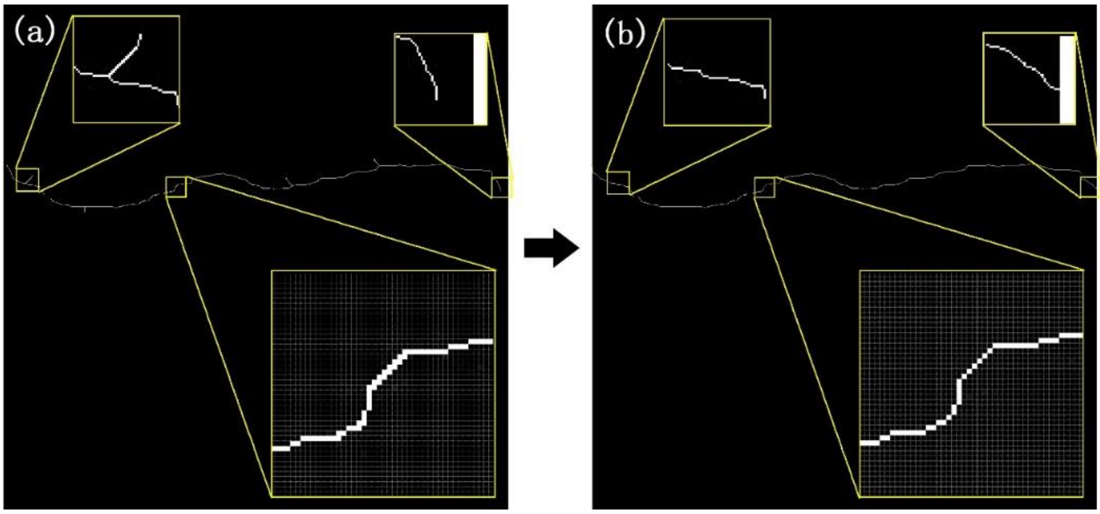

Fig. 5 Classic thinning algorithm (a) compared with the improved backbone refining algorithm in this study (b)

2.3 Determining the crack width measurement direction

As shown in Fig. 6, there are multiple measurement schemes that rely on the same measurement position, O. The measurement schemes AE, BF, CG and DH are the width-measurement results obtained at position O in different measurement directions. Notably, they are quite different from each other. The width is measured along the normal direction of the crack-growth direction according to the visual inspection method commonly used by engineers in practice. Evidently, the solution BF is more suitable for characterizing the width of the crack at position O. The main objective of this section is to get as many measurement points as possible and determine the width of the crack in the visual measurement along the optimum measurement direction to closely approximate the width obtained by the commonly used method in practice.

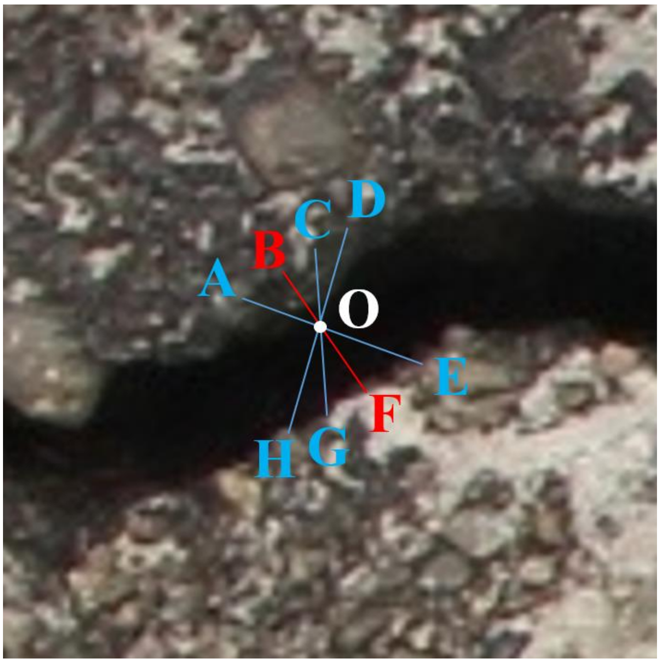

Fig. 6 Different measurement methods on the same crack

This paper proposes a method for determining the direction of crack width measurement based on the dual-scale features of the backbone. The proposed method combines the slope information of the crack backbone at the macroscale with its neighborhood information at the microscale. The macroscale information is based on the trend of the entire backbone of the crack, whereas the microscale information is based on the neighborhood distribution information of each pixel of the crack backbone. The combined method defines eight measurement directions, and then macro- and micro-scale information is matched to each of these eight directions. When the dual-scale information matches, the measurement direction can be determined and obtained. For points where the macroscale and microscale information do not match, the measurement is abandoned. Because the point where the direction is incorrect or cannot be measured will affect the reliability of the measurement result.

At the macro level, this study uses the least-squares method to fit the n-degree polynomial curve of the main stem into a polynomial function, $v = f(u)$, as established in Eq. (5):

$$\begin{bmatrix} v_1 \\ v_2 \\ \vdots \\ v_m \end{bmatrix} = \begin{bmatrix} 1 & u_1 & \cdots & u_1^n \\ 1 & u_2 & \cdots & u_2^n \\ \vdots & \vdots & \ddots & \vdots \\ 1 & u_m & \cdots & u_m^n \end{bmatrix} \times \begin{bmatrix} w_1 \\ w_2 \\ \vdots \\ w_n \end{bmatrix} \qquad (5)$$

$$\boldsymbol{V} = \boldsymbol{U} \times \boldsymbol{W}$$

where (u_m, v_m) is the coordinate value of the backbone point in the image coordinate system, W is the coefficient matrix of the polynomial function, m is the number of backbone points participating in the polynomial curve-fitting, n is the order of the highest degree of the curve, and $n = 9$.

The least-squares method is used to solve matrix W, as shown in Eq. (6):

$$\boldsymbol{W} = \left(\boldsymbol{U}^T\boldsymbol{U}\right)^{-1}\boldsymbol{U}^T\boldsymbol{V}. \qquad (6)$$

The first-order derivative of the function can be used to obtain the slope, dv_m, at any point on the backbone, as shown in Eq. (7):

$$dv_m = \sum_{i=1}^{n} a_{n-i} u_m^{n-i-1}. \qquad (7)$$

The angle, θ, between a straight line passing through any backbone point and the horizontal axis represents the measurement direction. This study defines eight measurement directions with an interval of 22.5° between each. At the macro level, mapping is defined from the slope, dv_m, of the curve, $v = f(u)$, to the macro measurement direction, ϕ, as shown in Eq. (8).

$$\phi = \begin{cases} 0°, dv_m \in (-\infty, \tan 101.25°) \cup [\tan 78.75°, +\infty) \\ 22.5°, dv_m \in [\tan 101.25°, \tan 123.75°) \\ 45°, dv_m \in [\tan 123.75°, \tan 146.25°) \\ 67.5°, dv_m \in [\tan 146.25°, \tan 168.75°) \\ 90°, dv_m \in [\tan \text{-}11.25°, \tan 11.25°) \\ 112.5°, dv_m \in [\tan 11.25°, \tan 33.75°) \\ 135°, dv_m \in [\tan 33.75°, \tan 56.25°) \\ 157.5°, dv_m \in [\tan 56.25°, \tan 78.75°) \end{cases}. \qquad (8)$$

At the microscale, there are only 16 types of eight-neighborhood distributions of backbone points, and the number is relatively small. The mapping from the backbone point to the microscale measurement direction, φ, can be defined according to the eight-neighbor distribution types, as shown in Eq. (9).

$$\varphi = \begin{cases} 0°, (p1 + p5 = 2) \vee (p6 + p8 = 2) \vee (p2 + p4 = 2) \\ 22.5°, (p1 + p4 = 2) \vee (p5 + p8 = 2) \vee (p1 + p5 = 2) \\ 45°, (p4 + p8 = 2) \vee (p1 + p4 = 2) \vee (p5 + p8 = 2) \\ 67.5°, (p4 + p7 = 2) \vee (p3 + p8 = 2) \vee (p3 + p7 = 2) \\ 90°, (p3 + p7 = 2) \vee (p4 + p6 = 2) \vee (p2 + p8 = 2) \\ 112.5°, (p2 + p7) = 2) \vee (p3 + p6 = 2) \vee (p3 + p7 = 2) \\ 135°, (p2 + p6 = 2) \vee (p1 + p6 = 2) \vee (p2 + p5 = 2) \\ 157.5°, (p1 + p6 = 2) \vee (p2 + p5 = 2) \vee (p1 + p5 = 2) \end{cases}. \quad (9)$$

In fact, using only the macro- or micro-scale information of the backbone for direction determination may cause a large direction error. On the one hand, the polynomial curve fitted at the macroscale is continuous and smooth, and it is difficult to accurately fit the growth morphology of the crack backbone, as shown in Fig. 7; the white dots constitute the crack's backbone and the orange line is the smooth curve after fitting. They do not exactly coincide. On the other hand, at the microscale, as shown in the lower left corner of Fig. 4, only three pixels are used as the basis for direction determination at a time, which is insufficient to express the current growth state of the crack. In the blue circle in Fig. 7, manual measurement should be carried out in the 45° direction. However, as shown in the red circle, if microscale information has been used for measurements, it is measured in the vertical direction. Similarly, in the green circle, the vertical direction should be followed when taking the manual measurement. However, as shown in the yellow circle, if macroscale information has been used, it is still measured in the 45° direction.

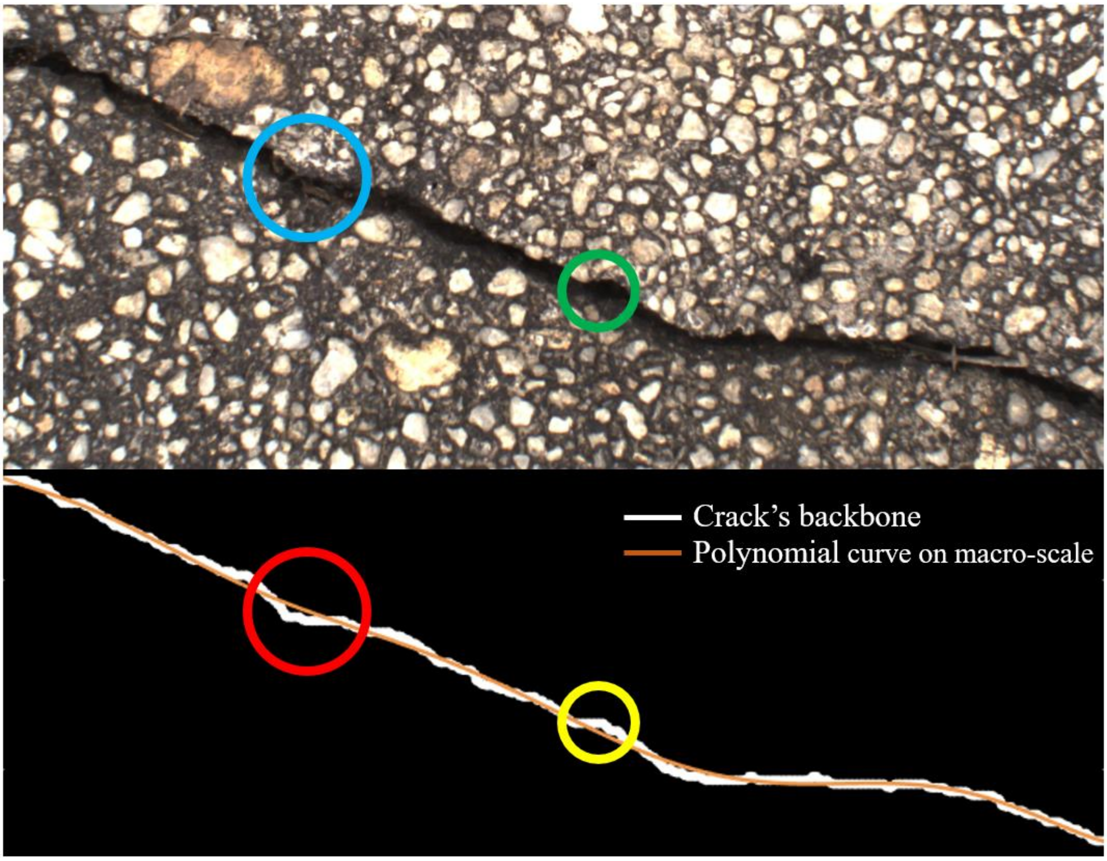

Fig. 7 Polynomial curve vs crack's backbone

Therefore, the measurement direction determination method must be designed to avoid errors in direction determination when using macroscopic or microscopic scale information alone. When solving the microscale direction, φ, this method is a situation where there are multiple neighborhood distribution types corresponding to one direction. Therefore, the microscale direction φ can be seen as a constraint on the macroscale direction, ϕ. When the macroscale, ϕ, and microscale, φ, directions of the backbone point are equal, the measurement direction, θ, of the point can be expressed as $\theta=\phi=\varphi$.

2.4 Crack width measurement

The straight line measurement, L_m, is defined according to the measurement direction and the main point, and the crack point (u_i, v_i) closest to L_m is found to form a point set, P_d, as in

Eq. (10):

$$P_d = \{(u_i, v_i) \mid |v_i - (\tan\theta * u_i + b)| < 1\}, \tag{10}$$

where b is the intercept of the linear equation, which can be obtained by substituting the coordinates of the backbone point into the equation.

The set P_d includes the upper edge measurement point, P_{mu}, and the lower edge measurement point, P_{md}, of the crack. As shown in Fig. 8, the yellow dots indicate the crack's backbone, the red dot is the measurement position at that place, the blue dots are P_d, and the green pixels are the two measurement points found according to the above method.

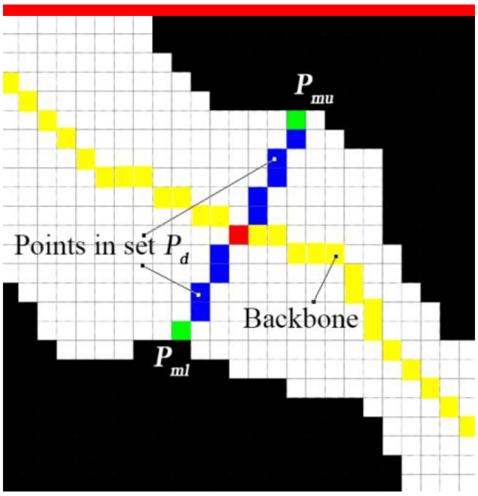

Fig. 8 Acquisition process for the measuring points

The values of P_{mu} and P_{ml} are shown in Eqs. (11) and (12):

$$P_{mu} \begin{cases} (u_{\max}, v_{\min}), 0° \le \theta < 90° \\ (u_{\min}, v_{\min}), 90° \le \theta < 180° \end{cases}, \tag{11}$$

$$P_{ml} \begin{cases} (u_{\min}, v_{\max}), 0° \le \theta < 90° \\ (u_{\max}, v_{\max}), 90° \le \theta < 180° \end{cases}. \tag{12}$$

As shown in Fig. 9, the blue line indicates the measurement method of the proposed method at this location, and the cracks covered by the blue lines can represent the range that can be measured on the crack image of this scheme.

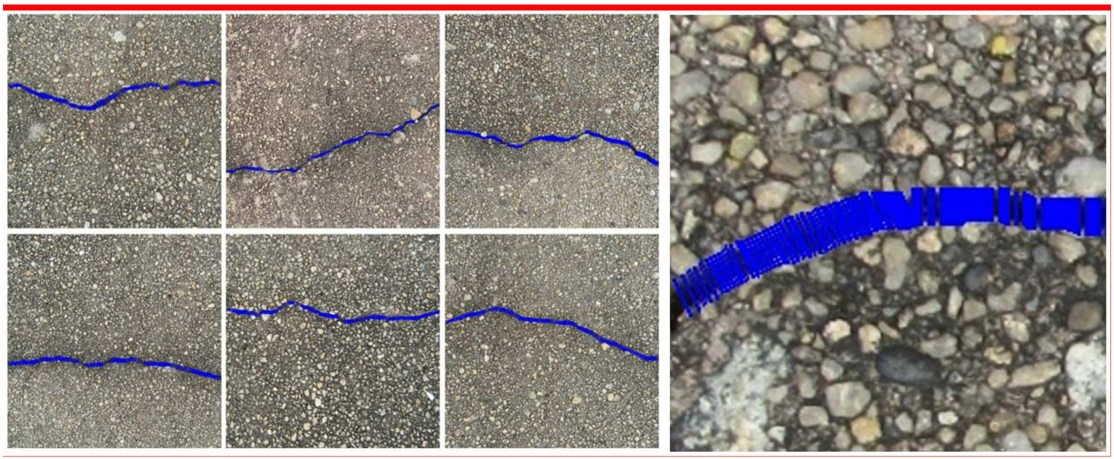

Fig. 9 Measurable point of a section of a crack and its measurement scheme

In this study, a binocular vision system is used for width-vision measurement, and the camera's sight axis is set perpendicular to the dam surface. Before measurement, the camera must be double-targeted to correct distortion and to perform epipolar line correction between the two cameras. Template matching is used to obtain four 50×50 image blocks on the right image corresponding to the upper-left, lower-left, upper-right, and lower-right of the left image. A four-dimensional vector, $\boldsymbol{uB}_i = [u_{Li} \quad v_{Li} \quad u_{Li} - u_{Ri} \quad 1]^T$, is constructed for the center of each image block $\left(u_{Li}, v_{Li}\right)^T$, representing the coordinates of the center point of the image block on the left image in the image coordinate system. u_{Li}-u_{Ri} represents the disparity value, d, of the center point of the same image block on the left and right images. The triangulation principle, $\boldsymbol{CB} = \boldsymbol{Q} \times \boldsymbol{uB}$, is used to obtain the coordinates, $\boldsymbol{CB}_i = \left(X_{Ci}, \ Y_{Ci}, \ Z_{Ci}, \ W_i\right)^T$, of the centers of the four image blocks in the camera coordinate system. Q is the reprojection matrix, which is obtained by the camera's dual objective setting, and $\boldsymbol{W}$ is a constant. The average of the four depth values indicates the average depth of the camera's optical center from the dam surface. Equation (13) is used to calculate the crack width, W_c, represented by the two measurement points, $P_{mu}\left(u_{mu}, v_{mu}\right)$ and $P_{md}\left(u_{md}, v_{md}\right)$.

$$W_c = \frac{\overline{Z}}{f_x \cdot f_y} \sqrt{f_y^{\,2} \cdot \left(u_{mu} - u_{md}\right)^2 + f_x^{\,2} \cdot \pi \left(v_{mu} - v_{md}\right)^2} \ . \tag{13}$$

Between these, f_x and f_y are the internal parameters of the camera, which represent the product of the physical focal length of the lens and the size of each unit in the x and y directions of the imaging device, respectively, which are obtained by camera calibration.

3 Test results and analysis

The test site of this study was Fenghuang Reservoir Dam in Conghua District, Guangzhou City, Guangdong Province. The dam of this reservoir has obvious cracks, and the samples are abundant. The test site is shown in Fig. 10.

For the crack backbone extraction algorithm, we set the reduction rate test to illustrate the performance of the algorithm when reducing the amount of data. To measure the performance of the direction determination method, we used the two evaluation criteria proposed in this study: the recall rate of the direction determination and the direction error, and the corresponding judgment method. A segmentation performance evaluation test and a width-vision measurement accuracy test were conducted. For the ground truth, we referred to the experiment in Section 4.2 of [26]. Six researchers marked the cracks; the direction of the crack width was the tangent direction of the commonly used crack growth, and the width was the distance between two points on the edge of the crack in the measurement direction.

Fig. 10 Test equipment and environment

3.1 Segmentation performance evaluation

A total of 5,760 sample images were used for training, all samples were randomly arranged, and the training, validation, and test sets were randomly allocated at a ratio of 6:2:2. For the training input and prediction output of the model, a square image with a resolution of 400 × 400 pixels was used. The Adam optimization algorithm was used in all relevant procedures.

For the trained U-Net model, commonly used semantic segmentation evaluation indicators were used (i.e., pixel accuracy [PA], average pixel accuracy [MPA], average intersection and combination ratio [MioU], and frequency weight intersection and combination ratio [FWIoU]) to evaluate the performance of U-Net segmentation for dam-crack evaluation. The evaluation was based on a test set having 1,152 images of dam cracks. The segmentation results of the model were decomposed to the original size of the test images via linear interpolation.

To evaluate the segmentation effect of U-Net, the crack segmentation effects of the common semantic segmentation networks, SegNet and DeeplabV3+ (with Xception and MobileNetv2 as the backbone networks, respectively), were added for comparison. The distributions of their performance evaluation scores are shown in Fig. 11, while visual comparisons are presented in Fig. 12. The abscissa is the order of the graph, and the ordinate is the score.

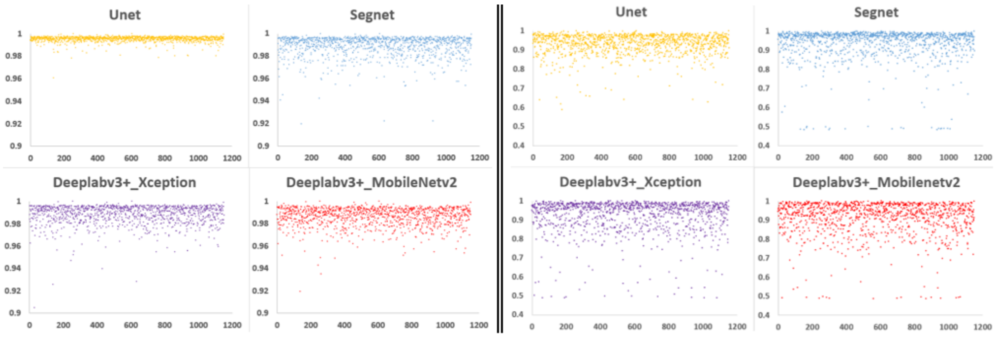

(a) PA (b) MPA

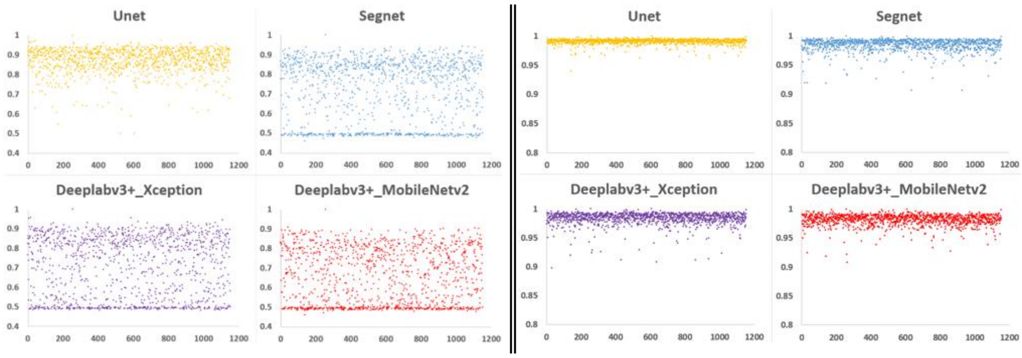

(c) MIoU (d) FWIoU

Fig. 11 Distribution comparison of the crack segmentation performance scores

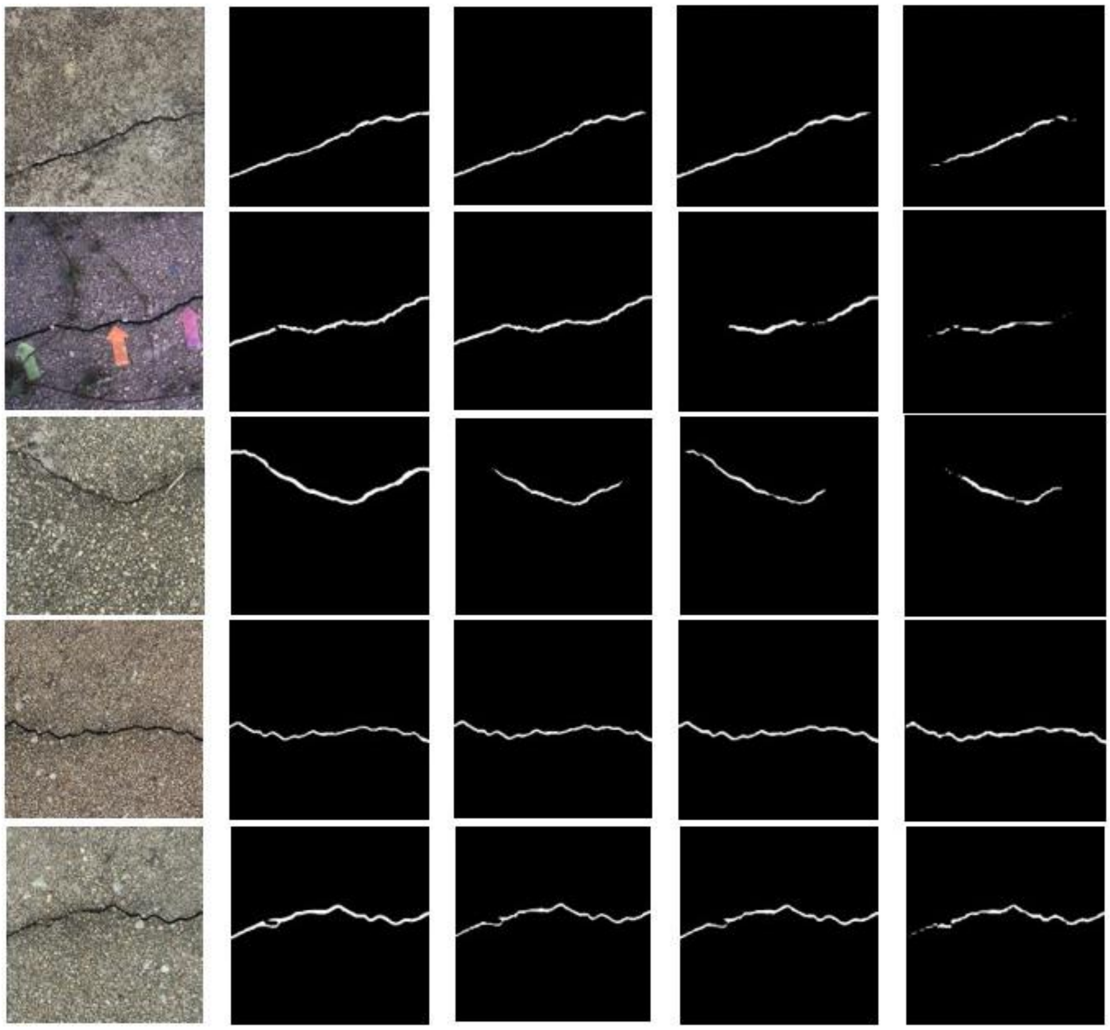

(a) Source (b) U-Net (c) SegNet (d) D+X (e) D+M

Fig. 12 Visual comparison of segmentation effects

The statistical results of the average and standard deviations of the performance evaluation scores are shown in Table 1.

Table 1. Statistics of the average and standard deviation of U-net performance evaluation scores

	PA		MPA		MIoU		FWIoU	
	Average	S.D.	Average	S.D.	Average	S.D.	Average	S.D.
U-Net	99.5 %	0.003	93.1 %	0.054	87.1 %	0.062	99.1 %	0.005
SegNet	98.9%	0.009	93.5%	0.084	72.5%	0.153	98.5%	0.010
D+X	98.8%	0.009	92.1%	0.087	70.8%	0.154	98.4%	0.011
D+M	98.6%	0.009	91.1%	0.089	65.8%	0.139	98.2%	0.010

* D+X is Deeplabv3+ with the backbone network of Xception, while D+X is MobileNetv2.

The results show that U-Net has higher segmentation accuracy and stability in the task of segmenting dam cracks than the other networks. Thus, a better improvement plan based on U-Net would be worthwhile. Consequently, U-Net segmentation results were directly used for subsequent width measurement in this study.

3.2 Evaluation of streamlining performance of crack backbone extraction algorithm

In this section, we compare the total number of backbone points (S_B , obtained by applying the backbone extraction algorithm) and the total number of skeleton points (S_S , obtained by applying the Zhang–Suen image-refinement algorithm) on the same crack segment to measure the streamlining performance of the crack backbone extraction algorithm proposed in this paper. The simplification rate of the crack backbone extraction algorithm relative to the Zhang–Suen image-refinement algorithm is R_e :

$$R_e = \frac{S_S - S_B}{S_S} \times 100\% . \tag{14}$$

Taking 100 randomly selected crack images as the samples in the experiment, the statistics of the results obtained are as shown in Fig. 13 and Table 2.

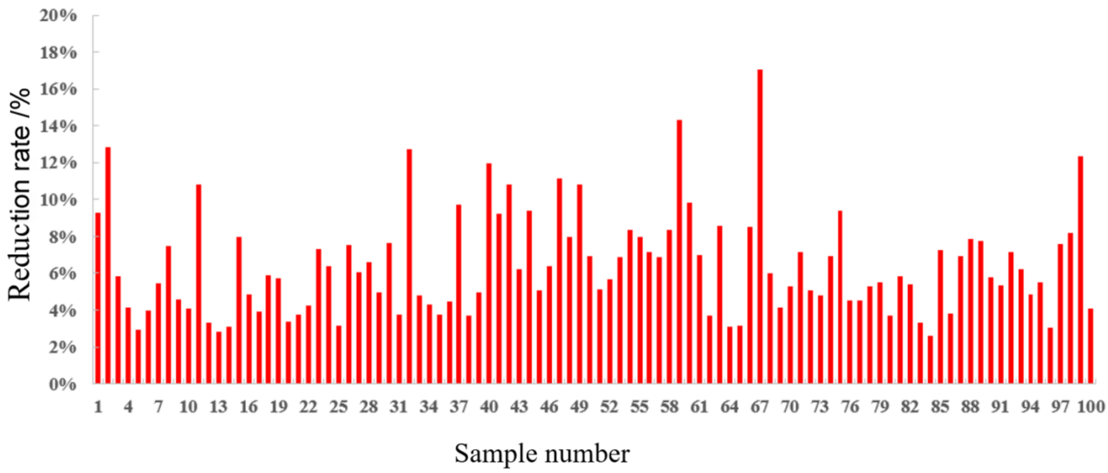

Fig. 13 Reduction rate test results

Table 2. Statistical results of the reduction rate test

	Mean	Median	Max	Min	S.D.
Reduction rate	6.40 %	5.82 %	17.04 %	2.60 %	3 %

As shown in Fig. 13 and Table 2, the skeleton obtained by the crack backbone extraction algorithm had an average simplification rate of 6.40 % compared with the skeleton obtained using the Zhang–Suen image-refinement algorithm. On the one hand, it showed that the skeleton obtained by the Zhang-Suen image thinning algorithm was universally spaced for further optimization. On the other hand, the measurement direction determination method in this paper was related to the eight-neighborhood pixel distribution of the backbone points, and the streamlining of the skeleton was conducive to the improvement of the matching degree of the macro- and micro-scale measurement direction information of the backbone. Thus, the streamlining performance was good. In addition, it is worth emphasizing that the crack backbone extraction algorithm proposed in this study had no more than two neighboring points for each backbone point, greatly reducing the number of backbone point neighborhood distribution types to only 16, which was convenient for classifying backbone points according to neighborhood distribution types.

3.3 Recall rate of direction determination method

The recall rate of the direction determination method refers to the ratio of the total length of each segment of cracks that can be visually measured in the width to the total length of the cracks in the image, which is used to investigate the recall performance of the measurement algorithm on the task of crack width measurement. On the other hand, the recall rate can also reflect the matching degree between the macro- and micro-scale information of the crack's backbone in the measurement direction determination problem in this method, because the backbone points of the macro- and micro-scale mismatch were the negative sample in the recall statistics. Number of pixels was used to approximate the length of the crack section. Using the direction determination method proposed in this study, the total number of measurable points, P_C, was obtained, and the total number of crack main points, P_S, was counted. The recall rate, R, is given by Eq. (15):

$$R = \frac{P_C}{P_S} \times 100\% . \tag{15}$$

In this study, 100 samples were randomly selected on the test set of U-Net crack segmentation, and the segmentation results were used as samples for the recall test. In addition, the control group used the same crack sample set, but the input of direction determination was the skeleton obtained by the Zhang–Suen thinning algorithm [53]. This was done to demonstrate the advantages of the proposed backbone extraction algorithm in the direction determination recall. The recall test results are shown in Fig. 14, where the red label represents the proposed method and the blue label represents the control group. The statistical results are listed in Table 3, where the label "Improved" represents the proposed method. The results show that the average recall rate of the proposed width-measurement direction determination method is approximately 74.90 %, and a standard deviation of 4 % indicated that the measurement was stable. They all outperformed the control group; the full-search performance was good overall. At the same time, the results show that the macro and micro information of the backbone points in the measurement direction determination problem were well matched, so that averaging three-quarters of the crack sections can make a more accurate measurement. More accurate here means that measurements with directions as a guide were theoretically more accurate than the measurement method which did not distinguish between measurement directions.

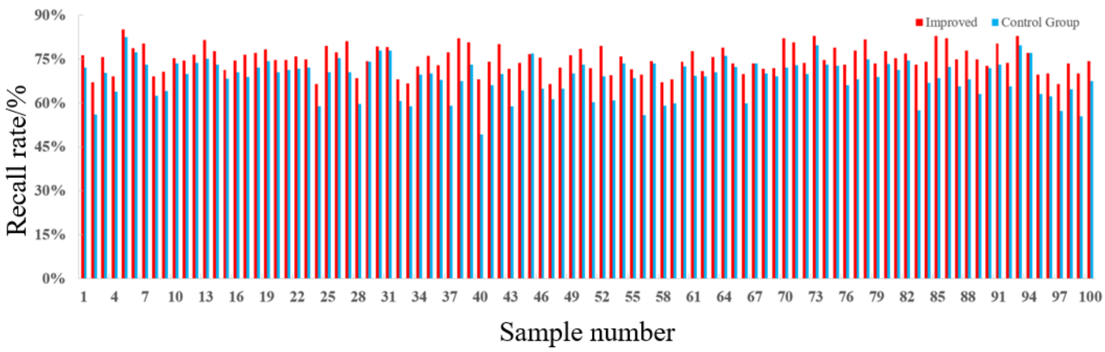

Fig. 14 Recall rate of the proposed width-measurement direction determination method

Table 3 Statistical results of the recall rate of the proposed direction determination method

	Mean	Median	Max	Min	S.D.
Improved	74.90%	74.73%	85.01%	66.36%	4%
Control Group	68.53%	69.82%	82.52%	49.24%	6%

3.4 Orientation error of width measurement direction determination

The direction error was used to evaluate the accuracy of the direction. We randomly selected 10 backbone points, P_{mi}, from the measurable points, and their positions were recorded and marked on the image. We invited three technicians to determine the measurement direction of the crack at the position marked on the image based on their experience, taking the tangential direction of the crack-growth direction as the measurement direction. Hence, pixel points A and B were selected on the two edges of the crack, and the mark point, P_m, had to be on the line section AB or as close to it as possible.

The width measurement direction determination method was used to determine the measurement direction of the mark point, P_{mi}, and the crack-edge points, C and D, were recorded in this direction. We composed vectors $\overrightarrow{AB}$ and $\overrightarrow{CD}$ to find the acute angle between them. $\Delta\theta$ represents the determination error of the measurement direction, as shown in Eq. (16).

$$\Delta\theta = \arccos\left(\frac{\overrightarrow{AB} \bullet \overrightarrow{CD}}{|\overrightarrow{AB}| \bullet |\overrightarrow{CD}|}\right). \tag{16}$$

From 30 sample images, 10 points were randomly selected for testing and compared with the method proposed by Luo et al. [46]. Fig. 15 shows the distribution of the test results.

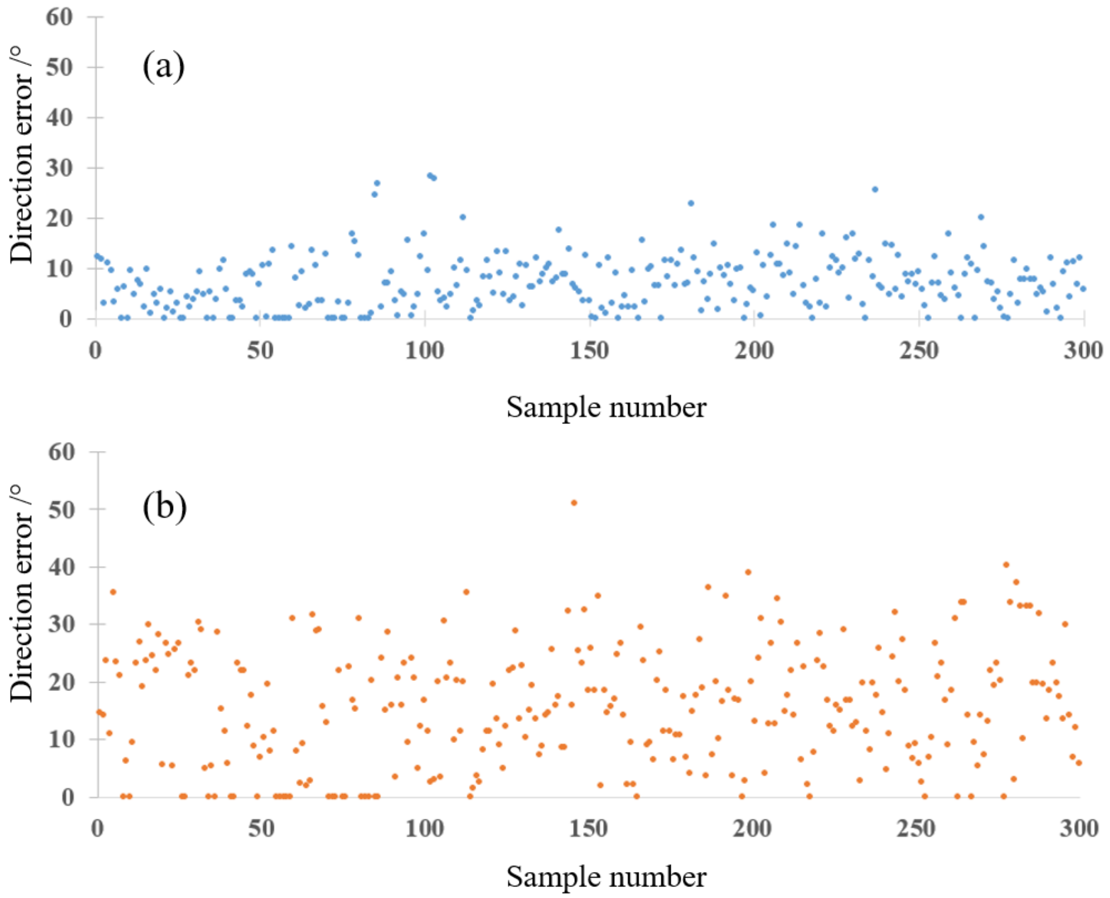

Fig. 15. Distribution of direction errors of width measurement direction determination methods: (a) proposed method; (b) method proposed by Luo et al. [46]

The statistical average, median, maximum, minimum, and standard deviation values are listed in Table 4.

Table 4. Direction error statistics of width measurement direction determination methods

	Mean /°	Median /°	Max /°	Mini /°	S.D. /°
Proposed method	6.97	6.45	28.10	0	5.39
Method proposed by Luo et al.[46]	15.44	15.09	51.01	0	10.25

The direction error of the proposed direction determination method was 6.97°, the median was 6.45°, the standard deviation was 5.39°, and the direction error did not exceed 28.10°, which is significantly better than the method by Luo et al. [46]. The above experiments show that the proposed method to determine the width measurement direction has practical accuracy and stability.

3.5 Test platform accuracy

The spatial distance between the two corner points of the calibration board was calculated by visual measurement and compared with the actual distance, which can be used to reflect the measurement accuracy of the test platform in this study. The calibration board was placed on the dam so that both the left and right cameras could shoot all corners while maintaining the state to continuously collect 200 images of the calibration board at 2 s intervals, correct them, and select 12 diagonal points on the board as sample points, as shown in Fig. 16.

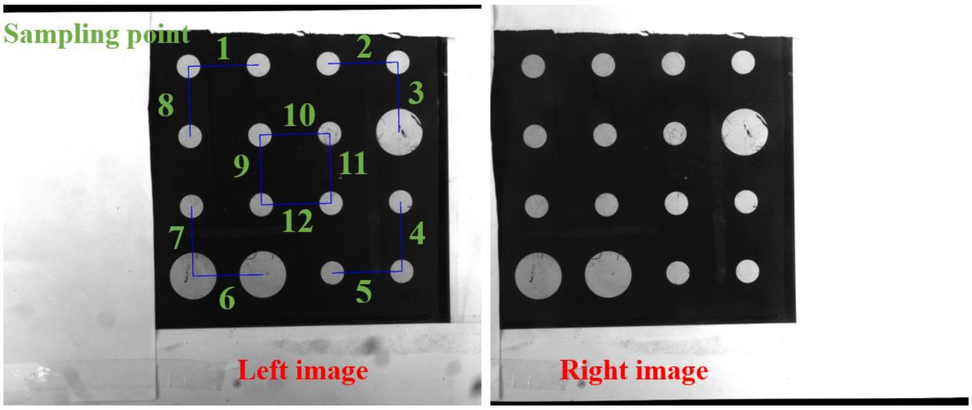

Fig. 16 Left and right images of the calibration board at the test site

The error between the visual distance measurement and the actual distance of each sampling point was used to determine the systematic error of the test device. In the experiment, the average ($\overline{\mu_B}$) and standard deviation (σ_B) of the error data, maximum absolute error (m_B) , average distance (R_B) from all repeated sampling points to the mean, and distance (D_B) between the maximum and minimum error data were used to evaluate the test device system error conditions. The results are presented in Table 5.

Table 5. Statistical value of the system error of the test device in this study

Serial number	$\overline{\mu_B}$	m_B	σ_B	R_B	D_B
Sampling point 1	0.007	0.035	0.011	-0.001	0.101
Sampling point 2	0.006	0.035	0.010	0.006	0.058
Sampling point 3	-0.001	0.024	0.010	-0.001	0.076

Sampling point 4	0.016	0.055	0.009	0.016	0.067
Sampling point 5	0.016	0.052	0.008	0.012	0.059
Sampling point 6	0.058	0.112	0.011	0.057	0.088
Sampling point 7	-0.004	0.0489	0.013	-0.004	0.082
Sampling point 8	0.006	0.044	0.013	-0.013	0.130
Sampling point 9	-0.033	-0.002	0.007	-0.033	0.083
Sampling point 10	0.018	0.048	0.010	0.018	0.059
Sampling point 11	0.040	0.071	0.014	0.040	0.059
Sampling point 12	-0.011	0.019	0.005	-0.011	0.062

The test results show that in the system error of the test device, $\overline{\mu_B}$, was basically zero, m_B did not exceed 0.12 mm, σ_B did not exceed 0.014 mm, R_B did not exceed 0.057 mm, and D_B did not exceed 0.13 mm. Thus, the test device had high accuracy and precision.

Fig. 17 shows the distribution of the error data. The horizontal axis represents the sampling sequence, and the vertical axis represents the measurement error in millimeters.

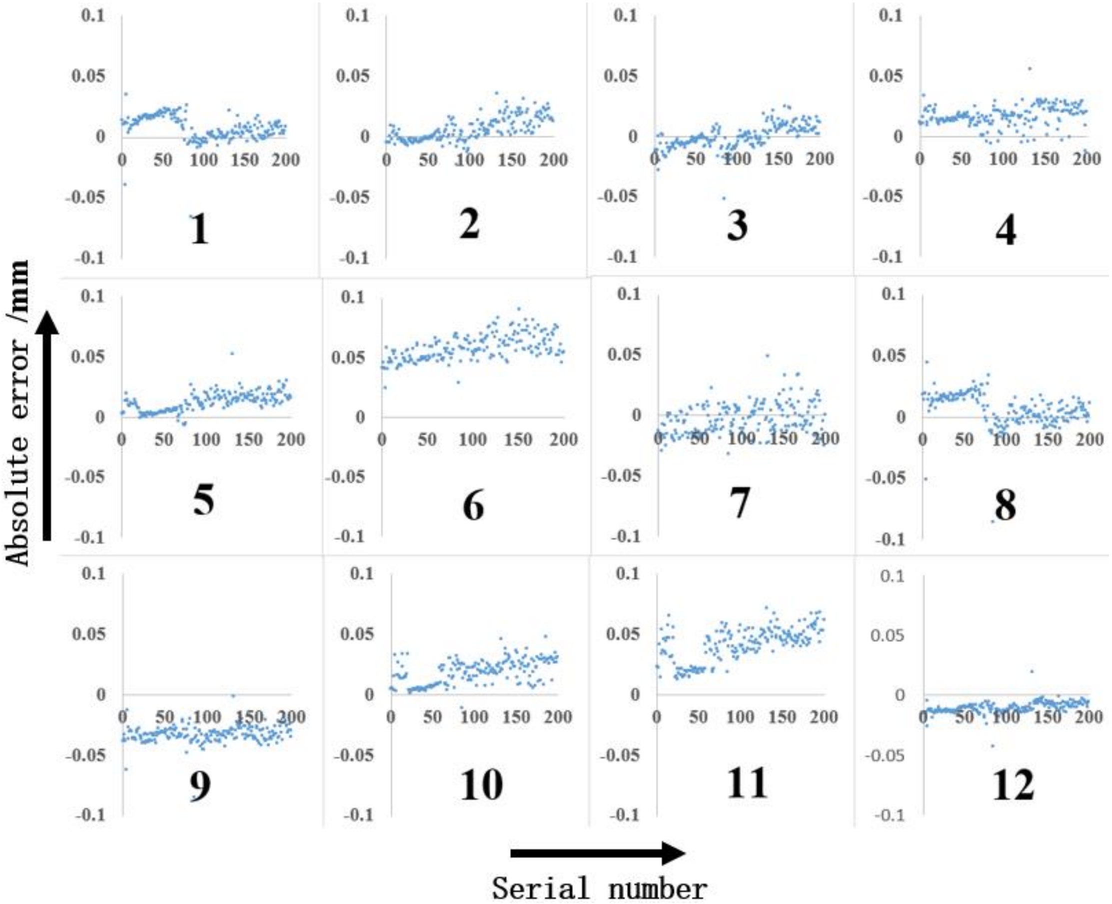

Fig. 17 Error distribution of repeated measurement sampling

3.6 Field width measurement test

The frame of the visual measurement test platform was constructed using aluminum profiles. The main equipment included two MV-EM510C industrial cameras (resolution 2,456 × 2,058), the focal length of the lens was 8 mm, and the distance between the camera lens and the dam surface was approximately 240 mm. When installed, the visual axis was perpendicular to the surface of the dam. A digital vernier caliper with an accuracy of 0.01 mm was used to measure the crack width on site for comparison data. The proposed algorithm for determining the measurement direction was used to obtain the measurable points in the crack. Then, five of the measurable points were randomly selected for width measurement, and the measurement position was marked in the real-time image of the left camera. Subsequently, the digital display vernier caliper was used to measure the inner diameter of the crack to obtain the standard value of its width at that location, as shown in Fig 18. The visual measurement value was used for comparison with the standard value. Referring to the experiments in previous studies [26,43,45], the absolute error was used to measure the accuracy of the proposed measurement method.

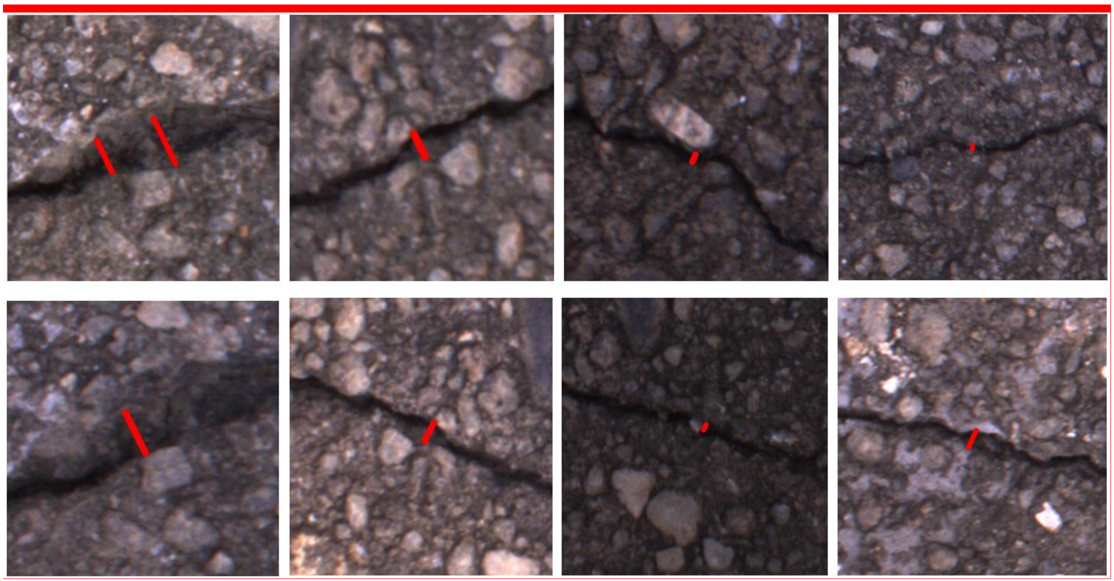

Fig. 18 Field measurement test

A total of nine groups were measured in this experiment. The deviation between the width value measured by the visual measurement and the standard value measured by the digital vernier caliper is shown in Fig. 19. The average absolute error, $\bar{\mu}$, and the standard deviation, σ , of the absolute error of each group of data are shown in Table 6.

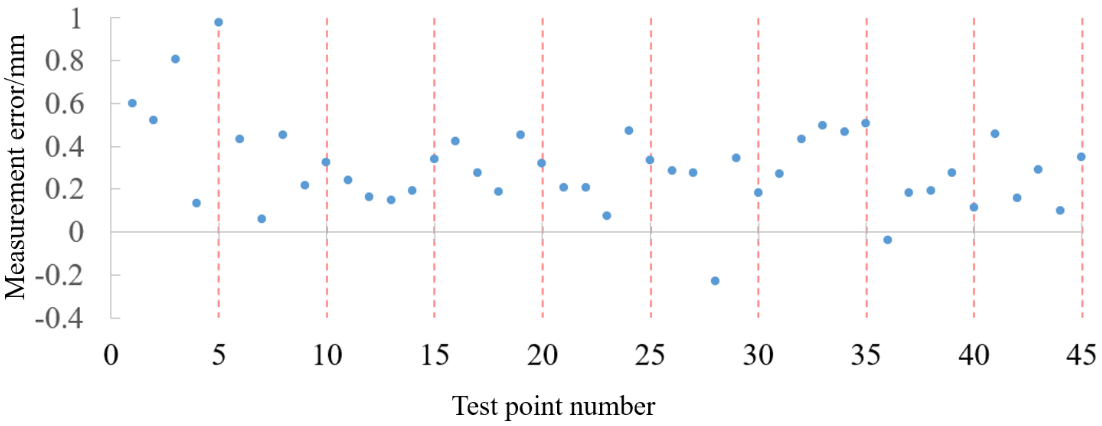

Fig. 19 Deviation of the width value of the visual measurement from the standard value

Table 6. Width measurement error average and standard deviation

Group	Error/(mm)	$\bar{\mu}$ /(mm)	σ /(mm)	Group	Error/(mm)	$\bar{\mu}$ /(mm)	σ /(mm)
	0.60				0.28		
	0.52				0.28		
1	0.81	0.61	0.32	6	-0.23	0.26	0.06
	0.13				0.35		
	0.98				0.18		
	0.43				0.27		
	0.06				0.43		
2	0.45	0.30	0.16	7	0.50	0.43	0.10
	0.22				0.47		
	0.33				0.51		
3	0.24	0.22	0.09	8	-0.04	0.16	0.09

	0.16				0.18		
	0.15				0.19		
	0.19				0.28		
	0.34				0.11		
	0.42				0.46		
	0.28				0.16		
4	0.19	0.33	0.11	9	0.29	0.27	0.14
	0.45				0.10		
	0.32				0.35		
	0.21						
	0.21				$\overline{\mu}$ mean = 0.32 mm		
5	0.07	0.26	0.15				
	0.47				σ mean = 0.19 mm		
	0.34						

In Fig. 19 and Table 6, the results show that the average error of this test was approximately 0.32 mm, and the average variance was 0.19 mm. This demonstrates that the visual measurement test results in this study are close to those of commonly used methods in engineering, which indicates that the proposed method can be utilized in engineering applications.

4 Conclusion

This study proposed a practical and complete visual method for measuring crack width using a real dam as the research object. The effectiveness of U-Net in the task of crack segmentation was first verified. Then, to address the problem of data redundancy in the crack skeleton, this study designed a more streamlined and stable crack backbone extraction method. The total number of eight-neighborhood points of each point on the backbone did not exceed two, which reduced the amount of backbone data and the distribution types of the eight neighborhoods of backbone points. The backbone's ability to describe the shape of cracks was also enhanced. Furthermore, we designed a more accurate method for determining the direction of the crack width measurement by combining the slope characteristics at the backbone macroscale feature and the neighborhood distribution characteristics at the microscale feature. We further defined the crack width visual measurement method according to the measurement direction.

To evaluate the advantages and disadvantages of the measurement methods, two criteria (i.e., recall rate of measurement direction and direction error) were added to provide a technical reference for subsequent research. Then, we conducted a series of experiments to verify that the proposed crack backbone extraction algorithm has a good streamlining effect compared to the Zhang–Suen image-refinement algorithm. Compared with the method presented by Luo et al. [46], we demonstrated that our proposed method obtains a more accurate width measurement direction. From the width measurement test, we also demonstrated that it has prospects for practical engineering applications, and the intelligent degree of structural health monitoring and repair was improved. The proposed method also provides a reference for the radial vision measurements of other slender and irregular targets.

In the future, for structural damage (e.g., cracks), research on faster, lighter, more accurate, and more stable image segmentation methods based on U-Net is needed. The visual measurement process should also be streamlined on the basis of the existing framework to improve the efficiency of the algorithm. Finally, the three-dimensional reconstruction of cracks should be explored to improve measurement accuracy and depth measurements so that vision systems will inherit more comprehensive crack-damage detection capabilities.

Acknowledgments

This research was funded by the National Natural Science Foundation of China (Grant No. U2006224, 52108199), China Postdoctoral Science Foundation (2021M690765), Science and Technology Planning Project of Guangzhou (202102080269), Natural Science Foundation of Guangxi Province (2021GXNSFAA220045), and Systematic Project of Guangxi Key Laboratory of Disaster Prevention and Engineering Safety (2021ZDK007).

Appendix A. Examples of processing procedures

Process	Result	Process	Result
Original		Binarized by U-Net	
Backbone refinement		Curve fitting in Macro scale	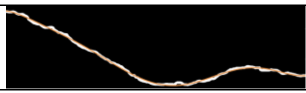
Distance to measuring surface	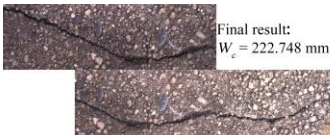	Width measurement	
P1(783, 1023)	Measurement point 1: (788,1013); Measurement point 2: (778,1033);	Measurement direction: 67.5° Width = 1.936 mm	
P2(1742, 1143)	Measurement point 1: (1731,1121); Measurement point 2: (1749,1158);	Measurement direction: 112.5° Width = 3.563 mm	
P3(1808, 1119)	Measurement point 1: (1796,1095); Measurement point 2: (1822,1148);	Measurement direction: 112.5° Width = 5.112 mm	
P4(2242, 1126)	Measurement point 1: (2242,1117); Measurement point 2: (2242,1140);	Measurement direction: 90° Width = 1.992 mm	
P5(2446, 1147)	Measurement point 1: (2446,1138); Measurement point 2: (2446,1156);	Measurement direction: 90° Width = 1.559 mm	

References

[1] G. Grzegorz, Evaluation of fracture processes under shear with the use of DIC technique in fly ash concrete and accurate measurement of crack path lengths with the use of a new crack tip tracking method, Measurement. (2021) 109632.

[2] H. Kim, E. Ahn, M. Shin, S.-H. Sim, Crack and noncrack classification from concrete surface images using machine learning, Structural Health Monitoring. 18 (2019) 725–738.

[3] C.-Z. Dong, F.N. Catbas, A review of computer vision–based structural health monitoring at local and global levels, Structural Health Monitoring. (2020) 1475921720935585.

[4] Q. Gong, L. Zhu, Y. Wang, Z. Yu, Automatic subway tunnel crack detection system based on line scan camera, Structural Control and Health Monitoring. (2021).

[5] B. Li, J. Yang, D. Hu, Dam monitoring data analysis methods: A literature review, Structural Control and Health Monitoring. 27 (2020) e2501.

[6] Z. Chen, X. Huang, S. Yu, W. Cao, W. Dang, Y. Wang, Risk analysis for clustered check dams due to heavy rainfall, International Journal of Sediment Research. 36 (2021) 291–305.

[7] E. Zhao, C. Wu, Risk probabilistic assessment of ultrahigh arch dams through regression panel modeling on deformation behavior, Structural Control and Health Monitoring. 28 (2021) e2716.

[8] D. Proske, Comparison of dam failure frequencies and failure probabilities, Beton-und Stahlbetonbau. 113 (2018) 2–6.

[9] X. Li, Z. Li, R. Feng, S. Luo, C. Zhang, M. Jiang, H. Shen, Generating high-quality and high-resolution seamless satellite imagery for large-scale urban regions, Remote Sensing. 12 (2020) 81.

[10] Y. Tang, A. Zhang, L. Luo , G. Wang, E. Yang, Pixel-level pavement crack segmentation with encoder-decoder network. Measurement. 184 (2021) 109914.

[11] Z. Liu, B. Gao, G.Y. Tian, Natural crack diagnosis system based on novel L-shaped electromagnetic sensing thermography, IEEE Transactions on Industrial Electronics. 67 (2019) 9703–9714.

[12] J. Pang, H. Zhang, C. Feng, L. Li, Research on crack segmentation method of hydro-junction project based on target detection network, KSCE Journal of Civil Engineering. 24 (2020) 2731–2741.

[13] A. Kocherla, M. Duddi, K.V.L. Subramaniam, Embedded PZT sensors for monitoring formation and crack opening in concrete structures, Measurement. (2021) 109698.

[14] Y. Xu, Z. Zhou, B. Zhang, Application of bionic crack monitoring in concrete bridges, Journal of Highway and Transportation Research and Development (English Edition). 6 (2012) 44–49.

[15] H.N. Nguyen, T.Y. Nguyen, D.L. Pham, Automatic measurement of concrete crack width in 2D multiple-phase images for building safety evaluation, in: Asian Conference on Intelligent Information and Database Systems, Springer, 2018: pp. 638–648.

[16] S. Yu, J. Zhang, X. He, An advanced vision-based deformation measurement method and application on a long-span cable-stayed bridge, Measurement Science and Technology. 31 (2020) 065201.

[17] J.S. Lee, S.H. Hwang, I.Y. Choi, Y. Choi, Estimation of crack width based on shape-sensitive kernels and semantic segmentation, Structural Control and Health Monitoring. 27 (2020).

[18] B. Ferrer, J. Espinosa, D. Mas, A method to measure small local strains in concrete surfaces using its natural texture and image cross-correlation, Structural Control and Health Monitoring. 26 (2019) e2410.

[19] X. Shao, Z. Chen, X. Dai, X. He, Camera array-based digital image correlation for high-resolution strain measurement, Review of Scientific Instruments. 89 (2018) 105110.

[20] Y. Chi, L. Yu, B. Pan, Low-cost, portable, robust and high-resolution single-camera stereo-DIC system and its application in high-temperature deformation measurements, Optics and Lasers in Engineering. 104 (2018) 141–148.

[21] B. Pan, Digital image correlation for surface deformation measurement: historical developments, recent advances and future goals, Measurement Science and Technology. 29 (2018) 82001.

[22] X. Li, H. Shen, H. Li, L. Zhang, Patch matching-based multitemporal group sparse representation for the missing information reconstruction of remote-sensing images, IEEE Journal of Selected Topics in Applied Earth Observations and Remote Sensing. 9 (2016) 3629–3641.

[23] H. Perez, J. Tah, Deep learning smartphone application for real-time detection of defects in buildings, Structural Control and Health Monitoring. 28 (2021) e2751 .

[24] M. Chen, Y. Tang, X. Zou, K. Huang, L. Li, Y. He, High-accuracy multi-camera reconstruction enhanced by adaptive point cloud correction algorithm, Optics and Lasers in Engineering. 122 (2019) 170–183.

[25] Y.-C. Tang, L.-J. Li, W.-X. Feng, F. Liu, X.-J. Zou, M.-Y. Chen, Binocular vision measurement and its application in full-field convex deformation of concrete-filled steel tubular columns, Measurement. 130 (2018) 372–383.

[26] W. Wang, A. Zhang, K.C.P. Wang, A.F. Braham, S. Qiu, Pavement crack width measurement based on Laplace's equation for continuity and unambiguity, Computer-Aided Civil and Infrastructure Engineering. 33 (2018) 110–123.

[27] Q. Zou, Z. Zhang, Q. Li, X. Qi, Q. Wang, S. Wang, Deepcrack: Learning hierarchical convolutional features for crack detection, IEEE Transactions on Image Processing. 28 (2018) 1498–1512.

[28] A. Zhang, K.C.P. Wang, Y. Fei, Y. Liu, C. Chen, G. Yang, J.Q. Li, E. Yang, S. Qiu, Automated pixel-level pavement crack detection on 3D asphalt surfaces with a recurrent neural network, Computer-Aided Civil and Infrastructure Engineering. 34 (2019) 213–229.

[29] M. Wang, J.C.P. Cheng, A unified convolutional neural network integrated with conditional random field for pipe defect segmentation, Computer-Aided Civil and Infrastructure Engineering. 35 (2020) 162–177.

[30] A. Rezaie, R. Achanta, M. Godio, K. Beyer, Comparison of crack segmentation using digital image correlation measurements and deep learning, Construction and Building Materials. 261 (2020) 120474.

[31] N.-D. Hoang, Detection of surface crack in building structures using image processing technique with an improved Otsu method for image thresholding, Advances in Civil Engineering. 2018 (2018).

[32] Y. Noh, D. Koo, Y.-M. Kang, D. Park, D. Lee, Automatic crack detection on concrete images using segmentation via fuzzy C-means clustering, in: 2017 International Conference on Applied System Innovation (ICASI), IEEE, 2017: pp. 877–880.

[33] H. Kim, E. Ahn, S. Cho, M. Shin, S.-H. Sim, Comparative analysis of image binarization methods for crack identification in concrete structures, Cement and Concrete Research. 99 (2017) 53–61.

[34] A. Garcia-Garcia, S. Orts-Escolano, S. Oprea, V. Villena-Martinez, J. Garcia-Rodriguez, A review on deep learning techniques applied to semantic segmentation, ArXiv Preprint ArXiv:1704.06857. (2017).

[35] C.V. Dung, Autonomous concrete crack detection using deep fully convolutional neural network, Automation in Construction. 99 (2019) 52–58.

[36] Y.-J. Cha, W. Choi, Vision-based concrete crack detection using a convolutional neural network, in: Dynamics of Civil Structures, Volume 2, Springer, 2017: pp. 71–73.

[37] Y. Cha, W. Choi, O. Büyüköztürk, Deep learning-based crack damage detection using convolutional neural networks, Computer-Aided Civil and Infrastructure Engineering. 32 (2017) 361–378.

[38] H. Ju, W. Li, S. Tighe, Z. Xu, J. Zhai, CrackU-net: A novel deep convolutional neural network for pixelwise pavement crack detection, Structural Control and Health Monitoring. (2020) e2551.

[39] A. Zhang, K.C.P. Wang, B. Li, E. Yang, X. Dai, Y. Peng, Y. Fei, Y. Liu, J.Q. Li, C. Chen, Automated pixel-level pavement crack detection on 3D asphalt surfaces using a deep-learning network, Computer-Aided Civil and Infrastructure Engineering. 32 (2017) 805–819.

[40] A.A. Diana, N. Anand, A.G. Prince, A novel approach for thermal crack detection and quantification in structural concrete using ripplet transform, Structural Control and Health Monitoring. 27 (2020).
[41] M. Payab, R. Abbasina, M. Khanzadi, A brief review and a new graph-based image analysis for concrete crack quantification, Archives of Computational Methods in Engineering. 26 (2019) 347–365.
[42] Y. Yan, Z. Mao, J. Wu, T. Padir, J.F. Hajjar, Towards automated detection and quantification of concrete cracks using integrated images and lidar data from unmanned aerial vehicles, Structural Control and Health Monitoring. (2021) e2757.
[43] S. Qiu, W. Wang, S. Wang, K.C.P. Wang, Methodology for accurate AASHTO PP67-10–based cracking quantification using 1-mm 3D pavement images, Journal of Computing in Civil Engineering. 31 (2017) 04016056.
[44] A.H. Asjodi, M.J. Daeizadeh, M. Hamidia, K.M. Dolatshahi, Arc Length method for extracting crack pattern characteristics, Structural Control and Health Monitoring. (2020).
[45] H. Kim, J. Lee, E. Ahn, S. Cho, M. Shin, S.-H. Sim, Concrete crack identification using a UAV incorporating hybrid image processing, Sensors. 17 (2017) 2052.
[46] Q. Luo, B. Ge, Q. Tian, A fast adaptive crack detection algorithm based on a double-edge extraction operator of FSM, Construction and Building Materials. 204 (2019) 244–254.
[47] B. Dai, C. Gu, E. Zhao, K. Zhu, W. Cao, X. Qin, Improved online sequential extreme learning machine for identifying crack behavior in concrete dam, Advances in Structural Engineering. 22 (2019) 402–412.
[48] C. Feng, H. Zhang, H. Wang, S. Wang, Y. Li, Automatic pixel-level crack detection on dam surface using deep convolutional network, Sensors. 20 (2020) 2069.
[49] O. Ronneberger, P. Fischer, T. Brox, U-net: Convolutional networks for biomedical image segmentation, in: International Conference on Medical Image Computing and Computer-Assisted Intervention, Springer, 2015: pp. 234–241.
[50] S.L.H. Lau, E.K.P. Chong, X. Yang, X. Wang, Automated pavement crack segmentation using u-net-based convolutional neural network, IEEE Access. 8 (2020) 114892–114899.
[51] Z. Liu, Y. Cao, Y. Wang, W. Wang, Computer vision-based concrete crack detection using U-net fully convolutional networks, Automation in Construction. 104 (2019) 129–139.
[52] Z. Zhang, Q. Liu, Y. Wang, Road extraction by deep residual u-net, IEEE Geoscience and Remote Sensing Letters. 15 (2018) 749–753.
[53] T.Y. Zhang, C.Y. Suen, A fast parallel algorithm for thinning digital patterns, Communications of the ACM. 27 (1984) 236–239.

Author statement

Yunchao Tang: Conceptualization, Methodology, Writing.

Zhaofeng Huang: Software, Validation.

Zheng Chen: Supervision, Editing.

Minyou Chen: Investigation, Reviewing.

Hao Zhou: Software, Editing.

Hexin Zhang: Editing, Validation.

Junbo Zhang: Data curation.

Editor and Reviewer comments: A major technical revision is needed. Should the authors decide to submit a revised manuscript, they should carefully and thoroughly address all comments offered by the reviewers, and reflect them in the revised manuscript. A point by point response must also be provided with the manuscript.

Reviewer #1:

This research studies the crack width measurement based on machine-vision systems. A backbone refinement algorithm and width-measurement scheme are proposed in this work. The research topic is interesting and within the scope of the Journal. However, from the perspective of the reviewer, the innovation of the proposed approach is not outstanding, and the current manuscript cannot be recommended for publication until the following concerns are carefully addressed.

1. The match of macroscale and microscale information in crack width measurements is significant. Without the match, the proposed methods may appear to be abandoned. Therefore, could you please discuss how to guarantee this match between the microscale and macroscale within your proposed framework?

Thanks for your valuable comments. Revised as suggested.

In this method, there are multiple neighborhood distribution types corresponding to one direction in the microscopic scale information, which is equivalent to adding microscale constraints to the macroscale information, thereby reducing the probability of incorrectly judging the crack width and improving the reliability of the measurement. In fact, using only the macro- or micro-scale information of the backbone for direction judgment may cause a large direction judgment error. Macroscale information is obtained using n-degree polynomials for curve fitting, and the result is a smooth curve, while the crack backbone in the natural state is not a smooth curve, as shown in the newly added Fig.7. On the other hand, at the microscopic scale, only three pixels are used as the basis for directional judgment, which is also not enough to accurately express the growth state of the crack at that place. Therefore, the design method of this paper uses the two-scale information fusion as the basis for judging the measurement direction. The supplement has been added in lines 275-293.

2. The U-Net is an existing method for crack recognition. The innovation of the whole framework is not outstanding. The advantages of the proposed approach should be demonstrated more clearly.

Thanks for your valuable comments. Revised as suggested.

U-Net was originally proposed to deal with the problem of image segmentation of retinal nerves with slender shapes, which has significance for the segmentation of cracks with equally elongated shape features. Previous researchers have used U-Net to study cracks and made progress in stages. By comparing other popular neural networks, this paper demonstrates that U-Net has the advantages of high accuracy and high stability compared with the neural networks used for comparison in crack detection, and has more application prospects. The focus of this article is on the visual measurement of cracks. More introductions to U-Net are supplemented on lines 122 to 129.

3. The figures are recommended to be modified in a more understandable manner. For the bar charts, e.g., Figure 14, the legends are expected to be added.

Thanks for your valuable comments. Revised as suggested.

Figures 4, 6, 7, 8, 9, and 14 have been modified and supplemented.

4. The difference between the proposed crack backbone extraction algorithm should be more clearly clarified in reference to other existing algorithms. In section 3.2, when evaluating the performance of the crack backbone extraction algorithm, please demonstrate the reason for the comparison of the simplification rate, why these indexes are important, and this improvement is significant.

Thanks for your valuable comments. Revised as suggested.

The biggest difference between the crack backbone in this paper and the skeleton extracted by other algorithms is that the crack backbone does not contain small branches, which can be used to express the fracture growth characteristics with more severe cracking. This is because, compared to the small crack branches, the crack backbone with a larger degree of cracking is more worthy of attention. Secondly, only the main crack was considered to make the extracted crack backbone more convenient to serve the width visual measurement, while avoiding the situation that the measurement direction is not unique in the same location. Simplifying the backbone to a single pixel structure is also an element of this research. The simplification rate can be quantified to show that it is meaningful to further study the crack backbone refinement from the general refinement algorithm. This is because after the refinement algorithm, on average, 6.4% of the pixels can still be refined further. The difference between the proposed crack backbone extraction algorithm and other existing algorithms has been added in line 155-158 and line 212-223. A description of the simplification rate has been supplemented in lines 407-416.

5. The recall rate in table reaches nearly 75%, which means the failure rate is still quite high. The samples in subsequent analyses are mentioned to be sampled randomly, but the corresponding results are no distinguished failure cases. Could you please explain the reason why there is no failure cases?

Thanks for your valuable comments. Revised as suggested.

Recall refers to the proportion of pixels on the backbone that can be used to judge the measurement direction. Recall statistics were based on pixels and were used to express the proportion of cracks that can be measured in the entire section, rather than the proportion of crack samples that were not successfully measured to the total sample. The remaining average 25% of the failure cases abandoned the measurement due to a mismatch between the two-scale features. Because the wrong measurement direction did not lead to the correct measurement results, abandoning these positions increased the credibility of the measurement results. Random sampling was done at a measurable location. The procedure did not contain points where the direction of the measurement could not be judged. The purpose of random sampling for measurement was to compare the error between the visual measurement and the actual manual measurement, and the identity case in this section was counted by the measurement direction error and the numerical error of the measurement result. Supplemented on lines 421-424 and 433-444.

6. Finally, the manuscript needs thorough proof reading by a native speaker.

Thanks for your valuable comments. Revised as suggested.

Reviewer #2: In the opinion of the reviewer, this paper is not appropriate for Engineering Structures. Indeed, a detailed description of the way of measuring the crack width is presented, without any correlation with the structural behavior of concrete elements.

Dear reviewer, thanks for your concern. We submitted this paper to the Special Issue "Machine Learning in Structural Engineering". And it fits one of the major interests.

Reviewer #3: This article describes an automated process for determining the width of cracks on the surface of concrete components. The process employs aspects of image analysis and machine learning. The work described by the authors appears to be scientifically sound and it has the potential to be useful to structural engineers who need to assess the cracking characteristics of existing concrete structures.

I recommend that the authors revise the manuscript to address the following concerns:

1. The authors should make the article more accessible to structural engineers who are not familiar with machine learning and image analysis, but who might want to apply the knowledge presented in the article. At a minimum, important technical terms that would not be known by most structural engineers should be defined. For example, it is not clear from the article what exactly is the difference between the "backbone" and the "skeleton". These and other terms need to be explicitly defined.

Thanks for your valuable comments. Revised as suggested.

The meanings of morphological processing, blurring, backbone and skeleton have been supplemented in lines 133-141, 155-158 and 214-225.

Among them, morphological processing here refers to dilation or erosion algorithms (they had opposite effects to each other), whose role is to expand the binarized target towards the background. The role of blur is also to expand the target, but its effect is more moderate than that of morphological processing.

2. The U-Net convolutional network is a key component of the process proposed by the article. Although the authors have correctly given the reference to the article by Ronneberger et al., I believe that U-Net will be unfamiliar to most structural engineers. I recommend that the authors include a brief description of the main features of this network.

Thanks for your valuable comments. Revised as suggested.

U-Net is a semantic segmentation network with 9 levels, which encodes and decodes images. The structure of the encoding stage and the decoding stage are symmetrical, and the shape is named U-shaped. The input of U-Net was an RGB image, and the output is a semantically segmented binary image in this article. The process of semantic segmentation takes place in a code-decoded symmetrical U-shaped structural model, hence the named U-Net. The acquisition of the parameters in the U-shaped structural model requires convolutional inference of a large number of labeled samples, which is then recorded in the model file. When used, the model file is called and the image data is passed into it. The segmentation result can be obtained after calculation by U-Net, which is a very simple and commonly used semantic segmentation model. Related introductions have been added in lines 123-129.

3. The authors consider both a macro-scale and a micro-scale basis for determining the slope of the "backbone" and hence the direction for determining crack width. They should provide a clear explanation of why both scales need to be considered. The significance of the macro-scale basis is fairly clear, given their approach to fitting a polynomial to the backbone and computing its first derivative. The significance of the micro-scale basis is, however, not obvious. In addition, the authors state that then the macro-scale and micro-scale produce different values for the angles phi and psi, then measurement at the given point is abandoned. The authors should explain what this situation corresponds to in physical

terms, perhaps giving some examples of real images.

Thanks for your valuable comments. Revised as suggested.

Macroscopic scale information is obtained using n-degree polynomials for curve fitting, and the result was a smooth curve, while the crack backbone in the natural state was not a smooth curve, as shown in the newly added Fig.7. On the other hand, at the microscopic scale, only three pixels are used as the basis for directional judgment, which was also not enough to accurately express the growth state of the crack at that place. Therefore, the design method of this paper used the two-scale information fusion as the basis for judging the measurement direction. In this method, there were multiple neighborhood distribution types corresponding to one direction in the microscopic scale information, which was equivalent to adding microscale constraints to the macroscale information, thereby reducing the probability of incorrectly judging the crack width and improving the reliability of the measurement. In the blue circle of Fig. 7, manual measurement should be carried out in the 45° direction. However, as shown in the red circle, if microscale information has been used for the measurement, it was measured in the vertical direction. Similarly, in the green circle, the vertical direction should be followed for the manual measurement. However, as shown in the yellow circle, if macroscale information has been used to measure, it was still measured in the 45° direction. In fact, using only the macroscopic or microscopic scale information of the backbone for direction judgment may cause a large direction judgment error. The supplement has been added in lines 204-210, 243-252 and 275-293.

4. The article is not clear on whether the process determines crack width at as many points as possible along the "backbone" or only at points determined by human intervention. This needs to be clarified.

Thanks for your valuable comments. Revised as suggested.

This article is to measure the crack width at as many points as possible along the backbone. The process of determining points with human intervention was just part of the experiment and was used to compare the differences between algorithmic measurements and manual measurements. In practice, all points on the crack where width measurements can be taken should be treated. Supplemented on lines 236-239.

5. It would be helpful for the authors to include, perhaps in conjunction with the flowchart given in Figure 1, an example of how the process they describe actually works, using real images and real numbers. This could perhaps be put into an appendix.

Thanks for your valuable comments. Revised as suggested.

Appendices have been added. For details, please refer to the appendix chapter at the end of the article.Appendix A. Examples of processing procedures

Process	Result	Process	Result
Original		Binarized by U-Net	
Backbone refination		Curve fitting in Macro scale	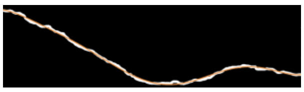

Distance to measuring surface	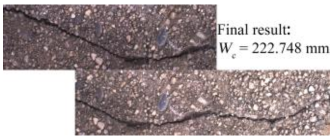	Width measurement	
P1(783, 1023)	Measurement point 1: (788,1013); Measurement point 2: (778,1033);	Measurement direction: 67.5° Width = 1.936 mm	
P2(1742, 1143)	Measurement point 1: (1731,1121); Measurement point 2: (1749,1158);	Measurement direction: 112.5° Width = 3.563 mm	
P3(1808, 1119)	Measurement point 1: (1796,1095); Measurement point 2: (1822,1148);	Measurement direction: 112.5° Width = 5.112 mm	
P4(2242, 1126)	Measurement point 1: (2242,1117); Measurement point 2: (2242,1140);	Measurement direction: 90° Width = 1.992 mm	
P5(2446, 1147)	Measurement point 1: (2446,1138); Measurement point 2: (2446,1156);	Measurement direction: 90° Width = 1.559 mm	

6. The article makes reference to the Zhang-Suen image-refinement algorithm, yet it is not clear what exactly is the difference between the "backbone" extraction algorithm described by the authors and the Zhang-Suen algorithm. This needs to be clarified.

Thanks for your valuable comments. Revised as suggested.

For the convenience of comparison and explanation in the following article, it is stipulated that the output of the Zhang-Suen image thinning algorithm is called “skeleton”, and the output proposed for improvement and further processing based on the Zhang-Suen image thinning algorithm in this article is called “backbone”. Compared with the classic Zhang-Suen image thinning algorithm, the crack backbone refinement algorithm in this paper has the following characteristics:

1. The effective neighborhood pixels of the backbone are less than 2, and there are only 16 types of neighborhood pixel distribution (as shown in the lower right corner of Fig. 4 and the lower right corner of Fig. 5);

2. The branches were removed and the shape of the end of the crack was retained (as shown in the upper left corner and upper right corner of Fig. 5).

The supplement has been added in lines 155-158 and 214-222.

[Sep. 12, 2022]

[Prof. Yang Jie]
[Editor-in-Chief]
[*ENGINEERING STRUCTURES*]

Dear Editor:

We wish to re-submit an origin article for publication in ***Engineering Structures***, entitled “Novel crack-width visual measurement based on backbone double-scale features.”

The manuscript has been rechecked and appropriate changes have been made in accordance with the reviewers’ suggestions. The responses to their comments have been prepared and attached herewith. The manuscript has been proofed by language edit center.

We thank you and the reviewers for your thoughtful suggestions and insights, which have enriched the manuscript and produced a better and more balanced account of the research. We look forward to working with you and the reviewers to move this manuscript closer to publication in ***Engineering Structures***.

Thank you for your consideration. We look forward to hearing from you.

Sincerely,
Yunchao Tang
School of Urban and Rural Construction
Zhongkai University of Agriculture and Engineering
Guangzhou, China
Email: ryan.twain@gmail.com

Chen Zheng
Key Laboratory of Disaster Prevention and Structural Safety of China Ministry of Education
School of Civil Engineering and Architecture
Guangxi University, Nanning, China 530004
[+86 13471196991]
[chenzheng@gxu.edu.cn]